NTIS # PB2022-

SSC-478
EXPERIMENTAL QUANTIFICATION OF THE TENSILE STRENGTH AND DUCTILITY OF UNDER-MATCHED ALUMINUM WELDS

This document has been approved
For public release and sale; its
Distribution is unlimited

SHIP STRUCTURE COMMITTEE

2022

Member Agencies:

American Bureau of Shipping
Defence Research & Development Canada
Maritime Administration
Military Sealift Command
Naval Sea Systems Command
Office of Naval Research
Society of Naval Architects & Marine Engineers
Transport Canada
United States Coast Guard

Ship Structure Committee

Address Correspondence to:

Commandant (CG-ENG-2/SSC)
ATTN: Executive Director, SSC
US Coast Guard
2703 Martin Luther King Jr. Ave SE
Washington, DC 20593-7509
Website: http://www.shipstructure.org

SSC – 478
SR – 1476

10 August 2022

EXPERIMENTAL QUANTIFICATION OF THE TENSILE STRENGTH AND DUCTILITY OF UNDER-MATCHED ALUMINUM WELDS

Under-matched fusion welds are a key challenge in the design of aluminum structures. The primary concern is that under extreme tensile loading, plastic deformation localizes in the under-matched region, leading to high strains and eventual ductile failure in these regions. Prior research has investigated the effect of under-matched welds in compression; however, the tensile properties had not been previously studied. The lack of published research into aluminum tensile design methods has left marine structural engineers without the practical tools and experimental data necessary to account for the impact of under-matched aluminum welds.

This study experimentally tested aluminum marine structural connections with under-matched welds in tension to better understand their characteristics and capabilities. The experimental results were used to develop a test database for future design method verification. This research confirmed that the heat-affected zones associated with under-matched welds significantly impact the strength of the connection and could affect the overall response of the structure.

We thank the authors and Project Technical Committee for their dedication and research toward completing the objectives and tasks detailed throughout this paper and continuing the Ship Structure Committee's mission to enhance the safety of life at sea.

W. R. ARGUIN
Rear Admiral, U.S. Coast Guard
Co-Chair, Ship Structure Committee

J. M. LLOYD
Rear Admiral, U.S. Navy
Co-Chair, Ship Structure Committee

SHIP STRUCTURE COMMITTEE

RADM Wayne Arguin
U. S. Coast Guard Assistant Commandant
for Prevention Policy (CG-5P)
Co-Chair, Ship Structure Committee

RDML Jason Lloyd
Chief Engineer and Deputy Commander
For Naval Systems Engineering (SEA05)
Co-Chair, Ship Structure Committee

Mr. Jeffrey Lantz
Director, Commercial Regulations and Standards (CG-5PS)
U.S. Coast Guard

Mr. Gareth Burton
Vice President, Technology
American Bureau of Shipping

Mr. H. Paul Cojeen
Society of Naval Architects and Marine Engineers

Dr. John MacKay
Head, Warship Performance, DGSTCO
Defence Research & Development Canada - Atlantic

Mr. Kevin Kohlmann
Director, Office of Safety
Maritime Administration

Mr. Luc Tremblay
Executive Director, Domestic Vessel Regulatory Oversight
and Boating Safety, Transport Canada

Mr. Albert Curry
Deputy Assistant Commandant for Engineering and
Logistics (CG-4D)
U.S. Coast Guard

Mr. Eric Duncan
Group Director, Ship Integrity and Performance Engineering
(SEA 05P)
Naval Sea Systems Command

Mr. Neil Lichtenstein
Deputy Director N7x, Engineering Directorate
Military Sealift Command

Dr. Thomas Fu
Director, Ship Systems and Engineering Research Division
Office of Naval Research

SHIP STRUCTURE EXECUTIVE GROUP & SUB-COMMITTEE

UNITED STATES COAST GUARD (CVE)
CAPT Daniel Cost
Mr. Jaideep Sirkar
Mr. Charles Rawson

AMERICAN BUREAU OF SHIPPING
Dr. Qing Yu
Dr. Gu Hai
Mr. Daniel LaMere
Ms. Christina Wang
Mr. Rich Delpizzo

SOCIETY OF NAVAL ARCHITECTS AND MARINE ENGINEERS
Mr. Frederick Ashcroft
Dr. Roger Basu
Dr. Robert Sielski
Dr. Paul Miller

DEFENCE RESEARCH & DEVELOPMENT CANADA ATLANTIC
Dr. Malcolm Smith
Mr. Cameron Munro
Mr. Neil Pegg

MARITIME ADMINISTRATION
Mr. Todd Ripley

TRANSPORT CANADA
Ms. Veronique Bérubé
Mr. Bashir Ahmed Golam
Ms. Tayyebe Seif

UNITED STATES COAST GUARD (FLEET)
CAPT Christopher Wolfe
Mr. Martin Hecker
Mr. Timothy McAllister
Mr. Debu Ghosh

NAVSEA/ NSWCCD
Mr. David Qualley
Mr. Dean Schleicher
Dr. Pradeep Sensharma
Mr. Daniel Bruchman

MILITARY SEALIFT COMMAND
Ms. Jeannette Viernes

OFFICE OF NAVAL RESEARCH
Dr. Paul Hess

PROJECT TECHNICAL COMMITTEE

The Ship Structure Committee greatly appreciates the contributions of the individuals that volunteered their time to participate on the Project Technical Committee, listed below, and thanks them heartily. They were the subject matter expert representatives of the Ship Structure Committee to the contractor, performing technical oversight during contracting, advising the contractor in cognizant matters pertaining to the contract of which the agencies were aware, and performing technical peer review of the work in progress and upon completion.

Chair:

Dr. Bob Sielski

Members:

Mr. Jason Cordell, USCG
Mr. David Qualley, NAVSEA
Mr. Marcus Cridland, American Bureau of Shipping
Keith Hennessy, Irving Shipbuilding
Dr. Paul Hess, Office of Naval Research
Ian Thompson, Defense Research and Development Canada

Ship Structure Committee Executive Director:

LCDR Bryan J. Andrews, U.S. Coast Guard

Technical Report Documentation Page

1. Report No. SSC-478	2. Government Accession No.	3. Recipient's Catalog No.
4. Title and Subtitle Experimental Quantification of the Tensile Strength and Ductility of Under-Matched Aluminum Welds		5. Report Date September 2020 6. Performing Organization Code
7. Author(s) Collette, M.		8. Performing Organization Report No. SR-1476
9. Performing Organization Name and Address University Of Michigan Marine Structures Design Lab 2600 Draper Drive Ann Arbor, Michigan 48109		10. Work Unit No. (TRAIS) 11. Contract or Grant No.
12. Sponsoring Agency Name and Address COMMANDANT (CG-5212/SSC) ATTN (ADMIN ASST/SHIP STRUCTURE COMMITTEE) U S COAST GUARD 2100 2ND ST SW STOP 7126 WASHINGTON DC 20593-7126		13. Type of Report and Period Covered Final Report 6/15-9/20 14. Sponsoring Agency Code G-M
15. Supplementary Notes Sponsored by the Ship Structure Committee. Jointly funded by its member agencies.		

16. Abstract

This work presents the in-plane response of a common aluminum shell-to-frame fillet weld connection. Such under-matched welds have not been extensively tested, even though they are critical for the structure's overall tensile response. A test program covering both 5086 and 6061 alloys, extensive base material characterization, as well as cross-weld hardness profiles and heat-affected zone (HAZ) characterization was completed. Eighteen specimens were tested varying weld size and alloy, with three replicates of each design. For 6061 specimens, weld heat input had a large impact on the resulting strength, while for 5086 specimens, the strength was reduced somewhat, but the results showed far less sensitivity to the weld heat input. Peak strength and approximate load-extensions curves, as well as data for future FEA and design method validation, are presented.

17. Key Words Aluminum welds, Heat affected zone, HAZ, Finite Element Analysis, Fillet		18. Distribution Statement Approved for public release; distribution is unlimited. Available from: National Technical Information Service Springfield, VA 22161 (703) 487-4650	
19. Security Classif. (of this report) Unclassified	20. Security Classif. (of this page) Unclassified	21. No. of Pages	22. Price

CONVERSION FACTORS
(Approximate conversions to metric measures)

To convert from	to	Function	Value
LENGTH			
inches	meters	divide	39.3701
inches	millimeters	multiply by	25.4000
feet	meters	divide by	3.2808
VOLUME			
cubic feet	cubic meters	divide by	35.3149
cubic inches	cubic meters	divide by	61,024
SECTION MODULUS			
inches^2 feet	centimeters^2 meters	multiply by	1.9665
inches^2 feet	centimeters^3	multiply by	196.6448
inches^3	centimeters^3	multiply by	16.3871
MOMENT OF INERTIA			
inches^2 feet^2	centimeters^2 meters^2	divide by	1.6684
inches^2 feet^2	centimeters^4	multiply by	5993.73
inches^4	centimeters^4	multiply by	41.623
FORCE OR MASS			
long tons	tonne	multiply by	1.0160
long tons	kilograms	multiply by	1016.047
pounds	tonnes	divide by	2204.62
pounds	kilograms	divide by	2.2046
pounds	Newtons	multiply by	4.4482
PRESSURE OR STRESS			
pounds/inch^2	Newtons/meter^2 (Pascals)	multiply by	6894.757
kilo pounds/inch^2	mega Newtons/meter^2 (mega Pascals)	multiply by	6.8947
BENDING OR TORQUE			
foot tons	meter tons	divide by	3.2291
foot pounds	kilogram meters	divide by	7.23285
foot pounds	Newton meters	multiply by	1.35582
ENERGY			
foot pounds	Joules	multiply by	1.355826
STRESS INTENSITY			
kilo pound/inch^2 inch$^{1/2}$(ksi$\sqrt{\text{in}}$)	mega Newton MNm$^{3/2}$	multiply by	1.0998
J-INTEGRAL			
kilo pound/inch	Joules/mm^2	multiply by	0.1753
kilo pound/inch	kilo Joules/m^2	multiply by	175.3

SSC Final Report: Experimental Quantification of the Tensile Strength and Ductility of Under-Matched Aluminum Welds

Author: Matthew Collette

Research Contributions from: Renee Wiwel, Jason McCormick, Kaihua Zhang, Claire Wincott, Hung-Chun Lin

MSDL Report Number: 2020-004

Date: September 2020

Abstract: This work presents the in-plane response of a common aluminum shell-to-frame fillet weld connection. Such undermatched welds have not been extensively tested, even though they are critical for the structure's overall tensile response. A test program covering both 5086 and 6061 alloys, extensive base material characterization, as well as cross-weld hardness profiles and heat-affected zone (HAZ) characterization was completed. Eighteen specimens were tested varying weld size and alloy, with three replicates of each design. For 6061 specimens, weld heat input had a large impact on the resulting strength, while for 5086 specimens, the strength was reduced somewhat, but the results showed far less sensitivity to the weld heat input. Peak strength and approximate load-extensions curves, as well as data for future FEA and design method validation, are presented.

Marine Structures Design Lab
Department of Naval Architecture and Marine Engineering University of Michigan, 2600 Draper Drive
Ann Arbor, Michigan 48109
msdl.engin.umich.edu

Table of Contents

1 Executive Summary 10
2 Introduction 11
2.1 Motivation 11
2.2 Literature Review and Previous Work 11
2.2.1 Literature Review 11
2.2.2 Previous FEA and simple model results 16
2.3 Objectives 21
3 Specimen Design 22
3.1 Design of NLCFWC Specimens 23
3.2 Design of Material Characterizations Coupons 26
3.3 Design of Hardness Coupons 26
3.4 Design of Fabrication Procedure 26
3.5 Development of Complex Cross-Weld Specimens 28
3.6 FEA Validation of NLCFWC 30
3.7 Experimental Validation of a Single NLCFWC 31
4 Specimen Fabrication and Test Procedure 32
4.1 Fabrication and Material Certifications 32
4.2 Final Specimen Configurations 34
4.3 Material Coupon Testing 34
4.4 Cross-Weld Hardness Profiles 35
4.5 NLCFWC and More Complex Connection Experiments 36
5 Results 38
5.1 Base Material Coupons at Different Orientations 38
5.2 Cross-Weld Hardness and Simulated HAZ 43
5.3 NLCFWC Specimens 46
5.3.1 Specimen A1 47
5.3.2 Specimen A2 48
5.3.3 Specimen A3 49
5.3.4 Specimen B1 51
5.3.5 Specimen B2 52
5.3.6 Specimen B3 53
5.3.7 Specimen C1 54

5.3.8 Specimen C2 55
5.3.9 Specimen C3 56
5.3.10 Specimen D1 57
5.3.11 Specimen D2 58
5.3.12 Specimen D3 59
5.3.13 Specimen E1 60
5.3.14 Specimen E2 61
5.3.15 Specimen E3 62
5.3.16 Specimen F1 63
5.3.17 Specimen F2 64
5.3.18 Specimen F3 65
6 Comparison with FEA and Design Methods 66
6.1 FEA Simulations 66
6.2 FEA Results 69
7 Discussion and Recommendations for Future Work 73
7.1 Discussion 73
7.2 Suggestions for Future Work 76
8 Conclusions 76
9 Acknowledgments 77
10 References 77

Table of Illustrations

Figure 1: Idealized Single-Zone HAZ Undergoing Deformation without Constraint (right image)17
Figure 2: 5083 Material (n=16), HAZ 50% of Base Strength 18
Figure 3: 6082 Material (n=32) HAZ 50% of Base Strength 19
Figure 4: 6082 Material (n=32) HAZ 80% of Base Strength 19
Figure 5: Comparison of Different Specimen Widths, n=32, HAZ = 50%. HAZ Width = 3t 21
Figure 6: NLCFWC Specimen Geometry..... 22
Figure 7: Specimen Table from ASTM Standard E8 ([36]) 24
Figure 8: Overall dimensions of the non-load carrying fillet welded connection along with the edge and spacing distances for the proposed bolt pattern..... 25
Figure 9: Overall square specimen configuration, showing fillet-welded flat bar 11.5" (292mm) from the end. 5/16" (7.9mm) continuous weld version is shown..... 27
Figure 10: Sample specimen layout on square specimen showing three large NLCFWC specimens and supporting specimens. Note that the distribution of specimen types B, C, D vary plate-to-plate to produce five specimens of each type. 28
Figure 11: Stiffener/Frame Intersection Specimen 29
Figure 12: Offset Load-Carrying Fillet Weld Connections Fillet welds were made where the plate intersects the T-stiffener web on the top and where the plate and flange overlap on the bottom 30
Figure 13: FEA Simulation of Failure 31
Figure 14: Unwelded Specimen Test Piece After Failure showing DIC Gear Setup..... 32
Figure 15: MTS 810 Machine Used for Material Coupon Testing..... 35
Figure 16: Clark CM-400AT Micro-Hardness Machine used for Weld Hardness Profiles..... 36
Figure 17: Load Frame for Large Specimen Tests 37
Figure 18: Location of Optotrak Markers for Specimen 38
Figure 19: Engineering Stress-Strain Curves for 5086 Material Coupons with Ramberg-Osgood Fits 41
Figure 20: Engineering Stress-Strain Curves for 6061 Material Coupons with Ramberg-Osgood Fits 42
Figure 21: Cross-weld hardness profile of 5086 specimen with 5/16 weld. Heavy dashed line is the average of all four specimens. The center of flat bar is at 0mm distance. 43
Figure 22: Cross-weld hardness profile of 5086 specimen with 3/16 weld. Heavy dashed line is the average of all four specimens. The center of flat bar is at 0mm distance. 43
Figure 23: Cross-weld hardness profile of 5086 specimen with chain weld. Heavy dashed line is the average of all four specimens. The center of flat bar is at 0mm distance. 43
Figure 24: Cross-weld hardness profile of 6061 specimen with 5/16 weld. Heavy dashed line is the average of all four specimens. The center of flat bar is at 0mm distance. 43
Figure 25: Cross-weld hardness profile of 6061 specimen with 3/16 weld. Heavy dashed line is the average of all four specimens. The center of flat bar is at 0mm distance. 44
Figure 26: Cross-weld hardness profile of 6061 specimen with chain weld. Heavy dashed line is the average of all four specimens. The center of flat bar is at 0mm distance. 44
Figure 27: HAZ Tensile Coupons of 5086 Plate 45

Figure 28: HAZ Tensile Coupons of 6061 Plate 45
Figure 29: Specimen A1 Before Testing 47
Figure 30: Specimen A1 Showing Failure at Weld Toe 47
Figure 31: Specimen A2 Before Testing 48
Figure 32: Specimen A2 Showing Failure at Weld Toe 48
Figure 33: Specimen A3 Before Testing 49
Figure 34: Specimen A3 Showing Failure at Bolt Holes 50
Figure 35: Specimen B1 Before Testing 51
Figure 36: Specimen B2 Before Testing 52
Figure 37: Specimen B2 Showing Failure at Weld Toe 52
Figure 38: Specimen B3 Before Testing 53
Figure 39: Specimen B3 Showing Failure in Bolting Region 53
Figure 40: Specimen C1 Before Testing 54
Figure 41: Specimen C1 Showing Failure at the Weld Toe 54
Figure 42: Specimen C2 Before Testing 55
Figure 43: Specimen C2 Showing Failure at the Weld Toe 55
Figure 44: Specimen C3 Before Testing 56
Figure 45: Specimen C3 Showing Failure at the Weld Toe 56
Figure 46: Specimen D1 Showing Failure at the Weld Toe 57
Figure 47: Specimen D2 Before Testing 58
Figure 48: Specimen D3 Before Testing 59
Figure 49: Specimen D3 Showing Failure at the Weld Toe 59
Figure 50: Specimen E1 Before Testing 60
Figure 51: Specimen E1 Showing Failure at the Weld Toe 60
Figure 52: Specimen E2 Before Testing 61
Figure 53: Specimen E2 Showing Failure at the Weld Toe 61
Figure 54: Specimen E3 Before Testing 62
Figure 55: Specimen E3 Showing Failure at the Weld Toe 62
Figure 56: Specimen F1 Before Testing 63
Figure 57: Specimen F1 Showing Failure at the Weld Toe 63
Figure 58: Specimen F2 Before Testing 64
Figure 59: Specimen F2 Showing Failure at the Weld Toe 64
Figure 60: Specimen F3 Before Testing 65
Figure 61: Specimen F3 Showing Failure at the Weld Toe 65
Figure 62: Abaqus FEA Model and Model Mesh 66
Figure 63: Vertical Deformations After Welding Simulation, Maximum about 2mm with Corresponding Angle of 0.5 Degrees from Flat 68
Figure 64: Residual Stresses After Welding Simulation, von Mises with Peak Red Color about 250 MPa 68
Figure 65: Boundary Conditions for Tensile Extension Load Steps in FEA Model 69
Figure 66: von Mises Stress State Near Peak Load, 5086 7.9mm Continuous Welds, Red Colors About 345 MPa 69
Figure 67: Load-Extension Comparison Between Simplified Experimental Average Displacement and FEA Model, 5086 7.9mm Continuous Welds 70

Figure 68: Load-Extension Comparison Between Simplified Experimental Average Displacement and FEA Model, 5086 4.8mm Continuous Welds 71
Figure 69: Load-Extension Comparison Between Simplified Experimental Average Displacement and FEA Model, 5086 4.8mm Intermittent Welds..... 71
Figure 70: Load-Extension Comparison Between Simplified Experimental Average Displacement and FEA Model, 6061 4.8mm Continuous Welds 72
Figure 71: Load-Extension Comparison Between Simplified Experimental Average Displacement and FEA Model, 6061 4.8mm Intermittent Welds..... 72
Figure 72: Load-Extension Comparison Between Simplified Experimental Average Displacement and FEA Model, 6061 7.9mm Continuous Welds 73

Table of Tables

Table 1: 2-D FEA Study Parameters 18
Table 2: Ultimate Tensile Strength of Base Material and HAZ [37]–[39] 25
Table 3: Chemical Composition of 5086-H116 Alloy reported by Hulamin, remainder is AL 33
Table 4: Mechanical Properties of 5086-H116 Alloy report by Hulamin..... 33
Table 5: Chemical Composition of 6061-T651 Alloy reported by Henan Mingtai Aluminum, remainder is AL 33
Table 6: Mechanical Properties of 6061-T651 Alloy report by Henan Mingtai Aluminum 33
Table 7: Final Specimen Numbering by Material and Weld Type 34
Table 8: Material Coupon Tests, True Stress-Strain Properties..... 39
Table 9: Material Coupon Tests, Engineering Stress-Strain Properties..... 40
Table 10: Simulated HAZ Material Properties 45
Table 11: Final Breaking Loads in kN..... 46
Table 12: Approximate Material Properties for Ramberg-Osgood Material Model for Continuous Welds (c) and Intermittent Welds (i)..... 67

List of Abbreviations

AWS	American Welding Society
DIC	Digital Image Correlation
FEA	Finite-element analysis
GTAW	Gas Tungsten Arc Weld
HAZ	Heat-affected zone
kN	Kilonewton
MIG	Metal inert gas welding
NLCFWC	Non-load carrying fillet weld connection
ONR	Office of Naval Research
SSC	Ship Structure Committee
UTS	Ultimate tensile strength

1 Executive Summary

Welding common marine aluminum alloys creates undermatched heat-affected zones (HAZ), which can significantly weaken the surrounding base material. The impact of such HAZ has been explored in compression, but almost no experimental investigations of such welds have been made for tensile response. In tension, such undermatched regions can concentrate plastic strains and reduce the overall ductility of the structure. This strain concentration could potentially impact the structure's ability to develop its full strength in ultimate limit states, especially where tensile ductility is assumed, such as in hull girder bending.

A small systematic series test program for fillet welds with their HAZ perpendicular to the applied tensile loading was conducted in this work. This test program used both 5086 and 6061 alloys to capture the impact of different alloy formulations on strength, extensive base material characterization, as well as cross-weld hardness profiles, and heat-affected zone (HAZ) characterization. Replicates of 5086 and 6061 base material specimens in three different orientations were tested. All the material showed significant anisotropy with respect to rolling or extrusion direction and were highly consistent specimen to specimen. Cross-weld hardness profiles showed increasingly severe hardness reduction with increasing weld heat input. Several pure-HAZ hardness and material property specimens were also tested, characterizing the change in the tensile stress-strain curve with different degrees of heat impact.

Eighteen large cross-weld specimens were tested with varying weld sizes, with three replicates of each design. These specimens had 150mm (6") wide sections along the welds to allow weld-direction constraint forces to build up. Failure loads varied between 288 kN and 406 kN. For the 6061 specimens, the weld heat input significantly impacted the resulting strength, with larger fillet weld sizes resulting in weaker connections. For the 5086 specimens, the strength was reduced somewhat, but the results showed far less sensitivity to the weld heat input. The results showed striking consistency between samples but confirmed that the HAZ significantly impacts the strength of the connection; the failure will be localized in the HAZ region as expected for this type of connection and may influence the overall response of the structure. FEA was shown to be able to approximate the response of these details with acceptable accuracy. Further investigations into these connections and modeling approaches appear warranted.

2 Introduction

2.1 Motivation

Recent naval acquisition programs have increasingly explored the use of aluminum alloys as primary hull girder structural material due to their low weight as compared to steel. Aluminum structures typically weigh a third to a half less compared to steel structures. This reduction in weight allows vessels to achieve higher service speeds and extend their endurance ranges. Aluminum also fairs better than steel in its corrosion resistance and manufacturability. Aluminum is more easily extruded into complex shapes in a safe and cost-effective manner. However, aluminum alloys have a lower elastic modulus than steel, and their non-linear stress-strain curves depend on the alloy and temper of the aluminum. Furthermore, heat introduced from welding can significantly reduce the strength of aluminum connections in regions surrounding the weld in both precipitation-hardened and strain-hardened alloys. Such regions are termed the heat-affected zone (HAZ). These differences in material properties prevent aluminum structure design from relying on steel structure methods. Recent Ship Structure Committee work has highlighted the benefits of aluminum while noting that more information on the performance of the HAZ regions is needed to improve design [1].

Aluminum's use as a structural material in the marine world continues to expand, making it more important to understand the difference between aluminum and steel. In the late 1990s-2010, numerous multihull commercial ferries were built out of aluminum, with lengths exceeding 100m by the end of that timeframe. Recent U.S. Navy applications have included the use of aluminum as the primary hull-girder material in the LCS-2 class vessels, as well as the EPF (formally JHSV) support vessels. Similar to commercial ferries, these are large vessels, over 100m in length, with the added complication of worldwide deployment. In such applications, primary hull girder strength becomes a driving limit state. In turn, the in-plane stress limit states on grillage components become critical to the overall vessel's strength. In most steel vessels, understanding this loading requires understanding the non-linear compression response of the structure, and the tensile responses are normally assumed to be similar to the material tensile stress-strain curve. However, the HAZ in aluminum complicates this tensile response. While much progress on the compressive strength of aluminum structures has been reported in the literature, information surrounding the heat-affected zone's (HAZ) impact on tensile strength and ductility is much more limited. An understanding of the HAZ's effect on these properties is necessary for the design of hull girders and shell plating on aluminum vessels.

2.2 Literature Review and Previous Work

2.2.1 Literature Review

The first major study of the response of fusion welds with modern alloys was that of Hill, Clark, and Brungraber [2], who published a comprehensive paper on the strength of welds. Using a single-block HAZ description coupled with measuring the deformation over a 250mm/10" gauge length (which thereby includes a significant amount of non-HAZ material), formulas for the

strength of butt welds and fillet welds were developed. Going beyond simple welds, strength formulas for structural members such as columns, beams, and plates were proposed, including proposals for methods of handling welds in the mid-region of columns in compression.

Under-matched welds in high-strength steels have also been studied. Sato and Toyoda conducted a series of studies on this problem, concluding that while ductility is reduced, it is possible to get near-strength matching even with weaker weld metal. Using a simplified notch representation, they explored the effects of joint geometry on weldment performance [3], [4]. A key finding from this work is that the constraint provided by the stronger base metal can raise the strength of the joint, especially when the joint is deep and narrow. For most aluminum applications, however, the HAZ tends to be fairly wide compared to the plate thickness, which is often less than 10mm. Broader studies of steel welds, including extensive finite element analysis and discussion of the impact of undermatch on other failure modes have been published by the Ship Structure Committee [5] as well as ASTM [6].

A study of butt welds in two common marine alloys, 5083 and 6082, was made by Scott and Gittos [7]. Scott and Gittos studied welds made with both 4043 and 5556 weld filler metals in 3mm and 13mm thick plates. Efforts were made to characterize the strength of the base material and weld material, with tension tests on specimens composed entirely of base material and weld material carried out along with cross-weld tension tests. Post-weld heat-treatments were also carried out on the 6082 welds. In general, fairly low elongations were observed; for the 3mm plate, overall elongations of 3 percent over a 5"/125mm gauge length were reported in the as-welded condition, reducing to as little as 1 percent if additional artificial aging was applied in post-weld heat treatment. Failure locations varied, including base metal, HAZ, and weld metal depending on the filler metal selected and any heat treatment applied. This work provided some of the first examinations of realistic welds in marine-type alloys and clearly shows how strain localization can impact the deformation capacities of 6xxx-series aluminum welds.

Several studies were made into 6082 beam-truss frameworks used in the oil industry on offshore platforms, including those of Övreas, Thaulow, and Hval [8] and Hval, Johnsen, Thaulow [9]. These two studies contain both experimental and numeric studies on welded connections, ranging from simple butt welds to complex beam joints under tensile loading. The welds were in 6082 material in both rolled and extruded conditions with plate thickness of 16mm, 35mm, and 50mm, joined with 5183 filler metal. Both studies addressed the concept of strain localization and examined how the lower overall ductility in these structures may conflict with classical plastic design rules. Constraint and tri-axial stress effects were seen to raise the strength of the joints, which were deeper and narrower than conventional vessel joints as the plates were much thicker than is typically seen in aluminum vessel construction. Hval, Johnsen, and Thaulow also noted that leaving the weld bead on the weld raised the amount of constraint in the HAZ near the weld and notably increased the strength of the weld. Hval, Johnsen, and Thaulow also present a summary of the shortcomings of then-existing design codes in assuring equal safety between conventional steel structures and aluminum structures with under-

matched welds, along with recommendations for designing aluminum structures that will minimize the impact of strain localization.

Malin [10] presented detailed studies of the microstructure of 6061-T6 gas metal arc welds in joining large extrusion panels. Malin studied a wide range of welding parameters on the same joint configuration. Malin determined that there were five different regions in the HAZ, and failure in the 6061-T6 HAZ originates in a narrow region of over-aged material with the lowest hardness in the HAZ. The hardness and width of this zone determines the overall strength of the joint, regardless of other impacts of the different welding parameters. Malin's results show that the joint failure dynamics are governed by local microstructures in the HAZ. This indicates that treating the HAZ as a uniform block or treating different aluminum alloys with a standard HAZ assumption is unlikely to reflect the response of different alloys.

Further tests on 6082-T6 welds were carried out by Matusiak [11], [12]. Matusiak carried out tests on both butt welds and load-bearing fillet welds, using 6082-T6 material welded with 5183 filler metal. For the butt welds, both 8mm and 20mm plates were used. As a part of this study, a series of small tensile specimens with cross-section dimensions 3mm x 4mm were cut parallel to the butt weld. Specimens were taken every 4mm off the weld centerline, allowing the material properties through the thickness of the HAZ to be studied. These specimens revealed that close to the weld metal, the HAZ had significantly less ductility than either the weld metal or the HAZ more remote to the weld. A series of cross-weld tension tests were developed, with the weld run at different angles to the applied stress. As expected, the case with the weld perpendicular to the applied stress had the lowest strength and deformation. Matusiak further investigated strength predictions using both simplified formulations and non-linear finite element studies. A key conclusion from the finite element study for the butt weld is that a tri-axial stress state is present in the weakest zone of the HAZ, and the strength of the weld is higher than the minimum material strength measured in the HAZ via the small material specimens. This tri-axial stress state is set up by the constraint of the surrounding, stronger material.

Chan and Porter Goff [13] investigated similar issues in welded plate-and-finger connections in tension members in a welded 7xxx-series alloy structure. Although 7xxx-series alloys have not been widely or successfully used in marine construction to date, the weldable 7xxx-series alloys have similar under-matched welds to 6061-T6 or 6082-T6 alloys. Chan and Porter Goff showed how strain localization impacts this type of tensile connector. Chan and Porter Goff proposed a simple analytical model of a finger-type tension connection joint, including characteristics of the base metal and different regions of the HAZ. This model was compared to finite element simulations of the joint and several experimental tension tests on similar joints, with generally good agreement. Lakshminarayanan et al. [14] presented a small study of butt welds in 6061 alloys, comparing friction stir welding to conventional welding. Results were broadly similar to those of Malin and Matusiak. As expected, the friction stir welded joints had higher hardness and strengths than the conventional welds.

Collette [15] examined the impact of welds on aluminum vessel structures, including a review of two simplified formulas to predict the tensile limit states of welded plates and panels. Neither method could predict all the experimentally observed responses. The impact of welds on hull-girder collapse limit states was also examined via an incremental curvature collapse model of an aluminum box girder. This study revealed that different types of idealization of the welds in the tension flange in the box girder could have a significant impact on the ultimate resisting bending moment developed by the box girder, and thus tensile weld limit states are important when capturing global responses. This work expanded a non-linear finite element study of different HAZ regions as part of ONR grant N00014-10-1-0193. Studying various models of the HAZ, the report concluded that through-thickness constraint forces were likely to be small for most marine welds, as the HAZ width is often 3-5 times the plate thickness. However, significant constraint does develop along the length of the weld, and narrow specimens may not capture the full extent of the HAZ response in a larger structure.

The desire to tie an understanding of the HAZ to the joint strength numerically has emerged as a key theme in modeling undermatched aluminum welds. Zhang et al. [16] provided one of the first major studies on this for welded aluminum auto body joints, taking microstructure predicted by the welding code WELDSIM and transferring it to Abaqus finite element models via an interpolation approach. While Zhang et al.'s work only compared to a single experimental test, it showed that such a combined numerical toolchain might be practical for weld strength simulation.

Another major numerical study on weld strength prediction was performed at NTNU, extending the earlier work of Matusiak by Wang [17]–[20]. Using a mixture of new hardness measurements and the micro-tensile test carried out previously by Matusiak, Wang studied numerical failure prediction in welds of 6082-T6, including load-bearing fillet welds, beam-column connections, and welded beams in bending. Using the non-linear finite element code LS-DYNA and shell element models, estimates of ductility and fracture loads were estimated, with generally good agreement between the experiments and the simulations. The Weak Texture Model using the anisotropic yield criterion of Barlat and Lian was used to capture the material parameters of the base material and HAZ regions in the model. However, the shell modeling approach proved to be mesh-sensitive, as the through-thickness stabilization stresses from constraints are not included. Wang developed and tested a non-local thinning model in LS-DYNA to capture this effect that significantly reduced the mesh sensitivity. Wang also proposed a simple analytical model for butt weld failure in rectangular plates. In general, the finite element approach proposed by Wang performed well, however identification of material parameters and use of the non-local thinning approach mean that the method requires significant set-up and analysis time to be applied to a welded joint. The work of Wang was further extended by Dørum et al. [21], who looked into both non-local thinning and cohesive zone approaches to modeling HAZ failure for vehicle crashworthiness. Dørum et al. also extended this approach to look at modeling the weld-induced material properties via simulation of the weld parameters through coupling the commercial numerical welding simulator WELDSIM to a specialty code NaMo that predicted microstructure evolution and then corresponding material properties. Vargas et al. [22] used FEA to focus on the heat profile of a

weld in 6061 aluminum and then correlated that heat input to experimental measurements. Hardness values and tensile properties were correlated for a number of experimental specimens.

Studies of the local microstructure and the ability to predict it numerically remain of strong research interest. Jakobsen's [23] master's thesis investigated the impact of changing 6082-T6 alloy composition on the hardness and microstructure of the HAZ after MIG welding. By varying the content of Mn, Cr, and Zr, it was hoped to change the HAZ microstructure and increase the alloy strengths. While changing the composition did change the amount of dispersoids in the HAZ after welding, this change did not translate into significant improvements in the as-welded properties. Deekhunthod [24] found similar results for 6005A alloys. Nazemi's [25] Ph.D. thesis numerically and experimentally studied aluminum welds. Using an FEA welding simulation, residual stresses, and phase transformation properties of 6000-series HAZ were predicted. A variety of experimental techniques then confirmed these readings. Weld failures were then modeled with the FEA simulations, using further experiments representative of a beam-column connection for validation. Digital image correlation was used to develop material constitutive models, and these were included in the FEA simulations. Overall, the work builds on that of Matusaik [11] and Wang [17] and shows that fully simulation-based evaluation of weld strength may be possible in the near future, as long as adequate material characterization is possible.

Brando et al. [26] examined the strength of aluminum column webs in tension, looking at situations where connections to columns in a building may cause failure. They adopted the same material models used in Matusaik [11] and Wang [17] for the weld HAZ. While they did not carry out additional experimental results, Abaqus FEA analysis revealed that the HAZ would play a significant role in the response of the joint. A simple formula, taking a ratio of non-welded and all-welded material properties, fit the FEA simulations well enough to be recommended for design purposes. Beyond the HAZ, the work also looked at the impact of column loads, as well as the material stress-strain curve and the degree of strain hardening available. Wiechmann et al. [27] present a detailed study of 6082 HAZ regions and weld metal via calorimetric approaches studying microstructure. Cross-weld strain distribution and hardness values are reported, and notably, for this material, the initial strain localization is in the weld itself, owing to lower flow stress than the weakest region in the HAZ. As the load increased, the weld material strain hardened, and the maximum strain shifted out into the HAZ. This result shows the complexity of the aluminum joint, though good agreement overall was observed between the welds and the carefully developed model.

Stathers et al. [28] studied the relationship between cross-weld hardness values and material strengths for 6061-T651 aluminum joined with gas metal arc welding. Using electrical discharge machining (EDM), small tensile coupons were machined approximately every 2mm through the HAZ. Regression equations were fitted from both Vickers and EQUOTIP hardness values. Good relationships were shown between hardness and both yield and tensile stress. The experimental results were confirmed via heat-treating different plates without welding and showing the hardness-strength relationships still matched those from the welded specimens.

Zheng et al. [29]–[31] studied the fracture of MIG welds in 6061 double-wall extruded panels from railcars. This work introduced a simpler method for calibrating numerical models of the weld material properties than taking micro-specimens, as was done by Matusaik [11] and Stathers et al. [28], primarily relying on simpler tension tests with more extensive instrumentation. Using a shear-based failure model for the material, excellent results were seen between the experimental fracture test and finite element predictions.

Chen and Guedes Soares [32] examined FEA modeling of aluminum welds, including the ability to predict residual stresses and distortions during the welding operations. Using experimental data from the 1980s, they showed that FEA simulations gave reasonable results and proposed a simple model to help model welding when full input temperature profiles are not available. Their model also showed the importance of updating the material properties with temperature, which significantly changed the residual stress distribution. This work did not examine the tensile response or the extent of the HAZ explicitly.

An FEA approach for larger structural models was proposed by Woelke et al. [33]. Based on previous work with cohesive zones for modeling large-scale ductile fracture as well as material failure in collision and grounding circumstances, a cohesive zone model was proposed for undermatched welds. The cohesive zone model replicates the complex failure in the HAZ, while the rest of the model can capture overall structural responses and deflections. This allows larger structural responses to be considered, as the FEA model does not need to rely on solid elements or enhanced shell elements for the region around the HAZ. As the properties modeled by the zone are effectively mesh-independent, significant freedom in constructing the global FEA model is obtained. Building off results from the earlier MIT study [30], a cohesive zone model was developed and validated for fracture of a 6061 aluminum weld in a large extrusion. If proper cohesive zone models are available, this approach allows rapid modeling of large aluminum structures.

2.2.2 Previous FEA and simple model results

The authors also completed a non-linear finite element study of different HAZ regions as part of ONR grant N00014-10-1-0193. The text and results that follow below are excerpted from the final report prepared under N00014-10-1-0193 and show the importance of correctly treating the HAZ regions. Non-linear finite element analysis of an idealized HAZ zone in isolation, ignoring any weld metal reinforcement, was made as a way of exploring the distribution of strain under uniform tensile extension. This model is highly simplified but represents, absent the weld, the situation encountered in most butt or non-load carrying fillet welds commonly used to assemble aluminum vessels. A picture of the idealization of the weld is shown in the left half of Figure 1.

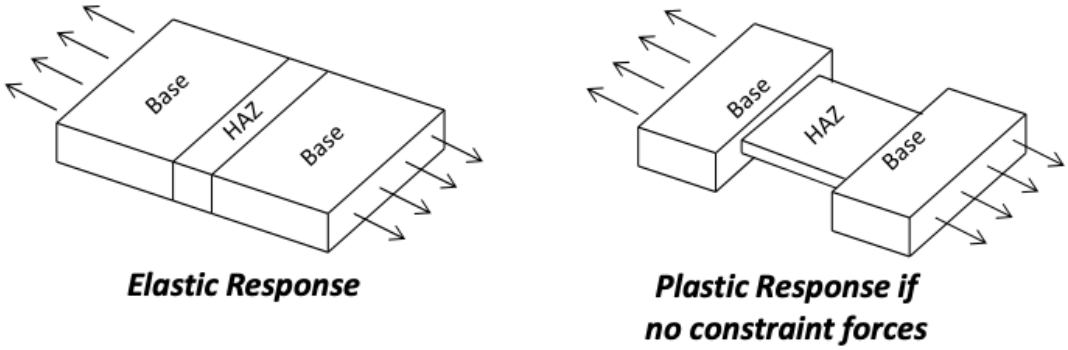

Figure 1: Idealized Single-Zone HAZ Undergoing Deformation without Constraint (right image)

Figure 1 shows a simplified schematic of a weaker HAZ region (ignoring any weld metal differences) surrounded by stronger base material. A key to understanding how the HAZ responds in tension is the concept of constraint. When loaded in tension, weaker HAZ material will deform plastically before the surrounding base material. In isolation, the plastic HAZ material would shrink both through the thickness of the plate and along the length of the weld. This situation is shown on the right-hand side of Figure 1. The HAZ is prevented from deforming in this manner by being fused to the still-elastic base metal. Thus, the base metal constrains the HAZ and induces a hydrostatic stress state in the HAZ material, which can retard yielding of the HAZ. The HAZ joint, therefore, appears stronger and stiffer than the HAZ material properties determined from small weld or coupon tests without adequate surrounding material. Both the work of Satoh and Toyoda[3], [4] and Dexter and Ferrell [5] provide a deep discussion and simplified models for considering such constraint forces.

Constraint forces are only partially represented in current FEA modeling techniques for marine structures ultimate strength. For example, the commonly applied shell elements do not have the capability to match through-thickness deformation along element boundaries. This indicates that a shell model will not include any through-thickness constraint forces. Thus, shell FEA models are not suitable for capturing this aspect of undermatched welds, regardless of mesh refinement, unless additional modeling techniques are applied via modified elements or the introduction of cohesive zones (e.g., the work of Wang [17] or Woelke et al. [33]).

Two and three-dimensional FEA models were made of potential HAZ configurations in 5083 and 6082 alloys, two of the commonly used high-strength aluminum alloys available today. These alloys differ significantly in their HAZ response; both lose a large percentage of their initial proof strength when welded, but the 5083 alloys still maintain a high ultimate strength in the HAZ while the 6082 alloys lose a large percentage of their ultimate stress as well. The parameters of the weld study were designed to cover the range of HAZ possible in 5083 and 6082 alloys and are captured below in Table 1. For all studies, the plate thickness was kept constant at 8mm, a half-length of 125mm (representative of a 10in/250mm weld specimen modeled with symmetry), and the base material had a proof stress of 260 MPa with an elastic modulus of 70000 MPa.

Table 1: 2-D FEA Study Parameters

Parameter	Values
Ramberg-Osgood Exponent	16, 32
HAZ Strength, % of base	50%, 60%, 70%, 80%, 90%
HAZ Width in terms of thickness	5t, 3t, 2t, 1.5t, 1t, 0.75t, 0.5t, 0.25

Sample results covering a range of the parameters are presented below in Figure 2 - Figure 4. In these figures, the 100% base material and 100% HAZ material lines were plotted based on the Ramberg-Osgood relation adjusted to plane strain conditions. The figures reveal a range of behaviors. As expected, the 6082 material, which does not strain-harden as effectively as the 5083 material, is more heavily impacted by the HAZ. In both materials, to get constraint forces large enough so that the joint approaches the performance of the base material, the HAZ must be very narrow and deep, with a maximum width of only 1/4 of the plate thickness. For the case where the HAZ is 50% of the base material strength, the strengthening from through-thickness constraint forces for HAZ typical of marine fusion welds (width of 3t) appears to be negligible. This indicates that the through-thickness constraint forces are generally expected to have a small impact on aluminum marine welds and can be ignored when doing larger-scale analysis.

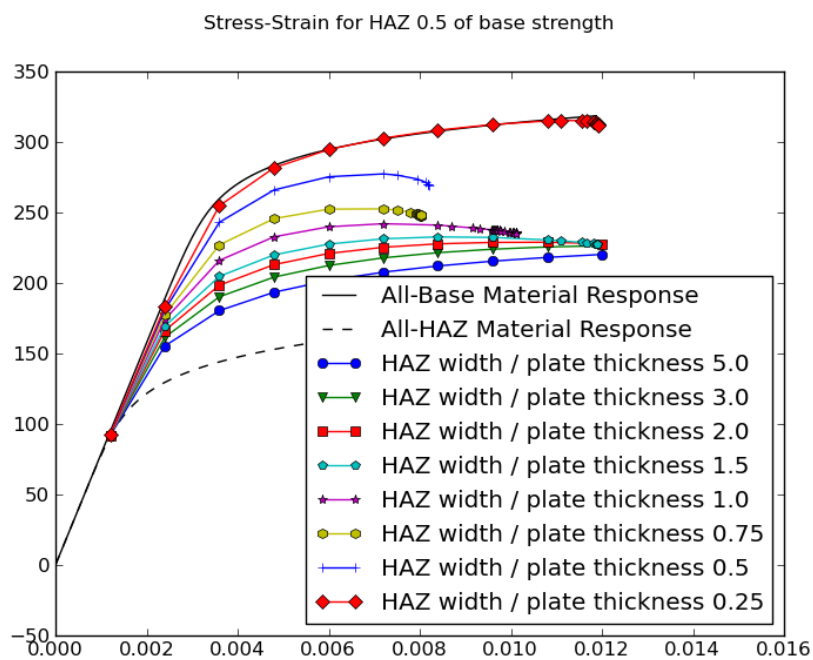

Figure 2: 5083 Material (n=16), HAZ 50% of Base Strength

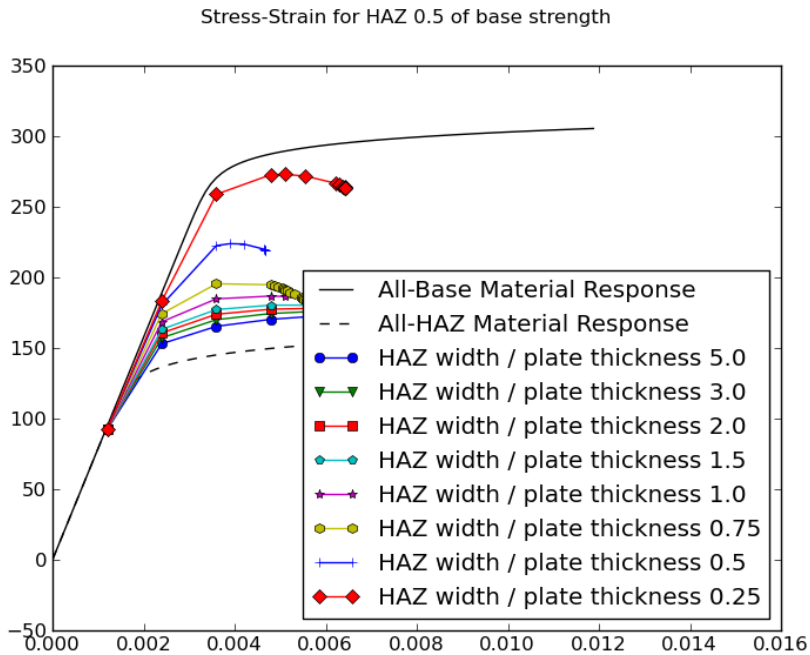

Figure 3: 6082 Material (n=32) HAZ 50% of Base Strength

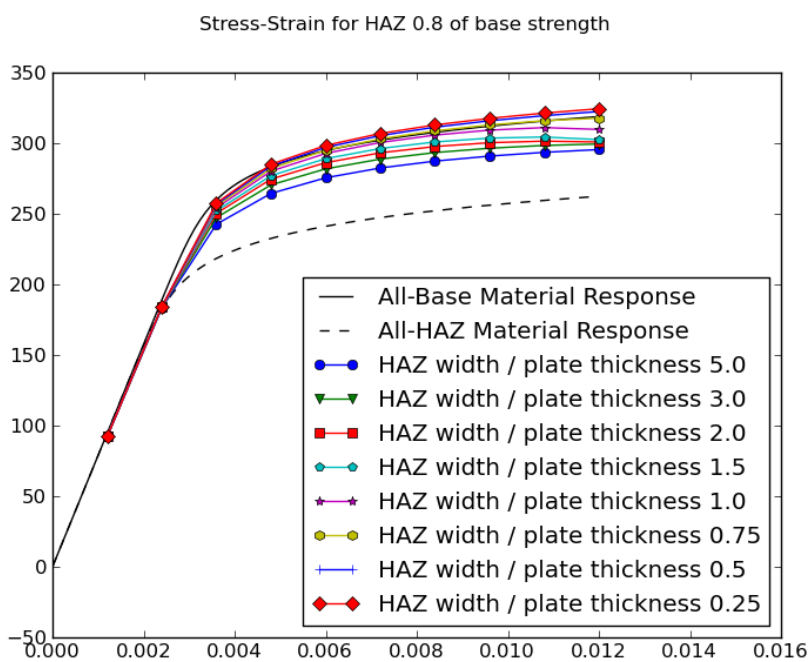

Figure 4: 6082 Material (n=32) HAZ 80% of Base Strength

A similar study was then made of the impact of constraint forces parallel to the direction of the weld. This was done by switching from 2-D FEA models to 3-D FEA models and increasing the width (or depth out of the plane of the page) to examine changes in constraint behavior. For

very shallow specimens, there is little restraint developed in the width direction, and the system approximates a plane-stress condition. As the width of the specimen increases, the HAZ metal in the center of the specimen is increasingly approaching a plane-strain condition, with correspondingly larger constraint forces. Based on the results of the 2-D plane strain models, the 6082 material with 50% HAZ strength was selected for analysis. A HAZ to plate thickness ratio of 3 was maintained, with the same 8mm plate thickness. Plate widths were varied over the following list: 8mm, 16mm, 32mm, 64mm, 128mm, and 256mm. The results were compared to a simple non-linear spring model of the joint with both plane-stress and plane-strain properties. In this model, it is assumed that each region (base metal, HAZ metal) in the joint responds independently following the Ramberg-Osgood relation. Only equal axial forces are maintained between regions. Mathematically, this can be stated as:

$$\epsilon_{\mathrm{total}} = \frac{\sum \epsilon_{\mathrm{i}} \mathrm{L}_{\mathrm{i}}}{\mathrm{L}_{\mathrm{total}}} \quad \textbf{(1)}$$

$$\epsilon_i = \frac{\sigma}{E_i} + 0.002\left(\frac{\sigma}{\sigma_{0.2i}}\right)^n \quad \textbf{(2)}$$

Where the subscript *i* indicates a material property specific to one zone of the model, with *E* indicating elastic modulus, $\sigma_{0.2}$ indicating proof stress, and *L* indicating length. The second part of this expression is simply the Ramberg-Osgood stress-strain equation being used as a non-linear spring model. The FEA results are compared in Figure 5. As soon as the specimen has any significant width, the results quickly begin to approach the plane-strain conditions. (Note that only the HAZ approaches plane strain as the width increases, as the outer edge of the model is always free, the base material does not. However, the base material remains largely elastic throughout the entire loading process). This indicates that it is generally safe to assume that along the direction of the weld, fully developed plane-strain restraint forces develop. Such forces can be captured by existing finite element shell modeling techniques if the HAZ is modeled in some detail.

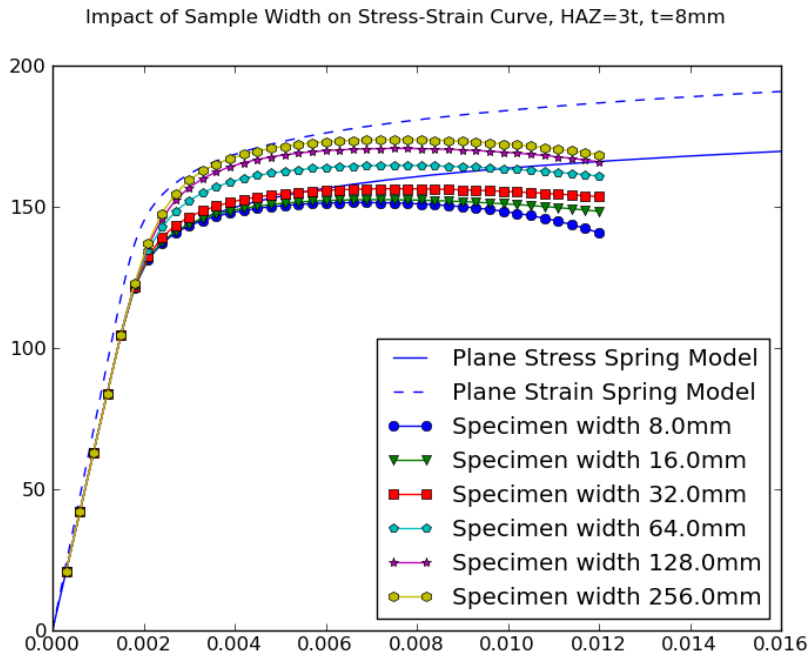

Figure 5: Comparison of Different Specimen Widths, n=32, HAZ = 50%. HAZ Width = 3t

The results from the initial parametric finite element study have been used to develop the current research plan. The presence of large along-the-weld constraint forces suggests that the current practice of testing small or even round specimens is missing a central aspect of the overall behavior of the weld specimens. Because of this, the actual as-built strength of the ship may be slightly higher than that forecast by small specimen testing, although the ductility may also be impacted. Ductility is a key component of the tensile response of ship structure, as high ductility is necessary to develop the full collapse strength for a thin-walled plate structure. Additionally, the simplified models used here did not include the notch effect of the weld reinforcement nor the local stress concentration typical in fillet-weld connections from the presence of the intersecting structural member. These factors would cause additional stress in the high-stress HAZ region. Therefore, experimental testing of typical marine welded connections is required to further study and understand these important regions.

2.3 Objectives

Based on the literature review, there is clearly a dearth of openly accessible experimental characterization of the impact of fusion welds on the tensile strength of marine aluminum structures. The objective of this project is to develop an experimental test database of undermatched aluminum welds relevant to marine vessel structures. This database should primarily be designed to allow further validation of analysis methods while secondarily shedding light on the performance of common weld types.

Based on this primary objective, a non-load carrying fillet weld connection (NLCFWC) was selected as the primary test focus on the experimental program. Such welds are common. For example, fillet welds connecting both longitudinals and transverse frames to the shell plate appear as non-load carrying fillet weld to stress fields primarily in the plane of the shell plate. Additionally, such welds are simple, allowing a relatively straightforward series of tests to be set up. A schematic view of a NLCFWC is shown in Figure 6. The following tests were set up around the concept of NLCFWC:

1. Eighteen parametric variations of NLCFWC, consisting of one alloy in the 5000-series and one alloy in the 6000-series. For each alloy, three different weld sizings and the three identical replicates of the specimen would be used.
2. Extensive material coupon data, taken from standard material coupon test specimens at 0°, 45°, and 90° to the rolling or extruding direction with five replicates of each specimen for each alloy and each direction.
3. Cross-weld hardness profiles to identify the extent of the HAZ for each alloy and weld type
4. Simulated HAZ specimens – by simulating different levels of thermal input along the plate, tensile specimens roughly corresponding to different regions of the HAZ can be generated to simulate the tensile response of the HAZ itself.

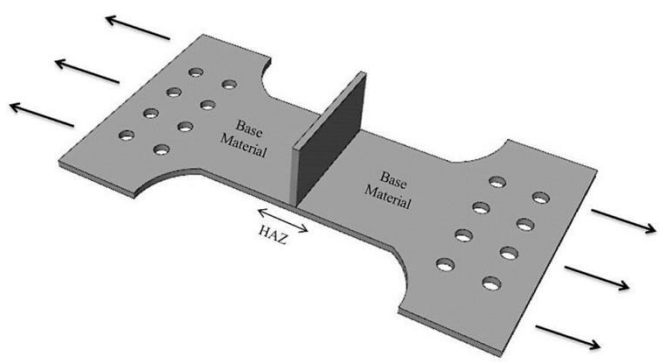

Figure 6: NLCFWC Specimen Geometry

Additionally, a more complex stiffener-frame intersection specimen and lap-shear joint similar to the ending of a double–wall extrusion will be tested. These will be fabricated from the same material types as the NLCFWC specimens but will represent more complex joints commonly used on larger aluminum structures. They will allow verification of finite element methods on more complex joints. In the end, grip limitations did not allow successful testing of these type of joints

3 Specimen Design

With the project objectives in mind, specific specimens were next designed that would allow the test program to achieve the objectives. Each type of specimen was first designed in isolation, which is reviewed below. Finally, a compact and simple fabrication design was

established that would allow rapid manufacture of all the specimens required. Before fabrication began, both FEA and a single one-off experimental test of a specimen were performed to validate the specimen design.

3.1 Design of NLCFWC Specimens

Based on the previous investigations of HAZ, the impact of the constraint of the surrounding base material is clearly important for the response of the overall connection. Thus, in designing the NLCFWC, a long HAZ region was desired. As many aluminum vessels use intermittent or chain welding, length in the HAZ region was also important to capture the response of such welds. Based on these considerations, and the available tensile testing machine size at the University of Michigan, a HAZ length of 6” was set as the target for the specimen. With the width, a 5/16” thick specimen was possible while maintaining reasonable overall breaking loads in the plate for both 5086-H116 and 6061-T651. Such as plate thickness is also well suited to representing many aluminum vessels, where shell plating may vary between 1/4” and 1/2”.

Based on the AWS *Guide for Aluminum Hull Welding* and the 2010 version of the *Aluminum Design Manual*, there are no specifications with regards to the maximum and minimum size of an aluminum fillet weld like there are for steel connections [34], [35]. However, the general rule in commercial work is that the size of the fillet weld is equal to the thickness of the thinner member in the connection [34]. Since both plates being joined are 5/16 inches thick, a 5/16 inch continuous fillet weld makes sense as the largest fillet weld to be investigated. This range of weld sizes is also broadly compatible with what is seen in the U.S. Navy’s guidance in NAVSEA S9074-A1-GIB-010/1628. A smaller fillet weld, 3/16 inch in size, will also be evaluated. Finally, an intermittent chain fillet weld 2 inches long with 1 inch of spacing between each weld will be tested. This intermittent chain weld guarantees that there are four inches of weld across each of the NLCFWCs so that the width of the reduced section of the test specimen exhibits the desired HAZ of approximately four inches and two inches of base material. The welds in the intermittent chain fillet weld variants would also be 3/16 inch in size. For all welds, the 5556 aluminum alloy will be used as weld filler material.

With the overall size and welds determined for the specimen, the next step was to determine the final geometry of the specimen for manufacture. The ASTM E8 1.50 inch wide plate-type and 0.50 inch wide sheet-type specimens shown in Figure 7 served as an initial design point for the proposed NLCFWCs and material coupons, respectively [36]. For the NLCFWCs with the 6” width in the middle of the specimen, the overall ASTM E8 specimen was adjusted by increasing the length of the grip section, and the radius of the fillet was increased so that a smooth transition existed between the reduced section and the grip section of the test specimen.

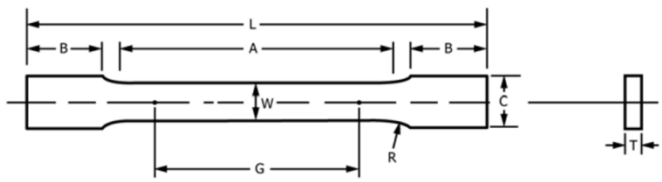

	Dimensions		
	Standard Specimens		Subsize Specimen
	Plate-Type, 40 mm [1.500 in.] Wide	Sheet-Type, 12.5 mm [0.500 in.] Wide	6 mm [0.250 in.] Wide
	mm [in.]	mm [in.]	mm [in.]
G—Gauge length (Note 1 and Note 2)	200.0 ± 0.2 [8.00 ± 0.01]	50.0 ± 0.1 [2.000 ± 0.005]	25.0 ± 0.1 [1.000 ± 0.003]
W—Width (Note 3 and Note 4)	40.0 ± 2.0 [1.500 ± 0.125, -0.250]	12.5 ± 0.2 [0.500 ± 0.010]	6.0 ± 0.1 [0.250 ± 0.005]
T—Thickness (Note 5)		thickness of material	
R—Radius of fillet, min (Note 6)	25 [1]	12.5 [0.500]	6 [0.250]
L—Overall length, min (Note 2, Note 7, and Note 8)	450 [18]	200 [8]	100 [4]
A—Length of reduced parallel section, min	225 [9]	57 [2.25]	32 [1.25]
B—Length of grip section, min (Note 9)	75 [3]	50 [2]	30 [1.25]
C—Width of grip section, approximate (Note 4 and Note 9)	50 [2]	20 [0.750]	10 [0.375]

Figure 7: Specimen Table from ASTM Standard E8 ([36])

Equation 3 was used to estimate the force, *F*, required for the test specimens to fail in tension. In this equation, *A* denotes the cross-sectional area of the reduced section of the test specimen and σ_u denotes the ultimate strength at the desired point of failure.

$$F = \sigma_u A \tag{3}$$

As the NLCFWCs are intended to fail in the HAZ, their ultimate strength was calculated as a weighted sum of the base material and HAZ ultimate strengths, as shown in Equation 4. This equation considers that there are 4 inches of HAZ and 2 inches of the base material along the connection for the chain intermittent weld to reflect the NLCFWC test specimen; the ultimate strengths of each region are weighted accordingly to determine the overall ultimate strength along the connection. Note that the ultimate tensile strength for the continuous weld variants would be less.

$$\sigma_u = \frac{4\sigma_{u_{HAZ}} + 2\sigma_{u_{Base}}}{6} \tag{4}$$

Table 2 lists the ultimate tensile strengths that were used to calculate σ_u for both the 5083 and 6061 aluminum connections [37]–[39]. Based on these inputs, the resulting breaking loads were 76.4 and 53.7 kips for the 5083 and 6061 alloys, respectively, of the chain intermittent fillet, welded connections; these breaking loads correspond to approximately 340 kN for the 5083 alloy and 239 kN for the 6061 alloy. Note that the NLCFWC with continuous welds would have lower breaking loads. Therefore, the test specimens are designed for the case with the highest breaking load (i.e., the chain intermittent fillet welded connections).

Table 2: Ultimate Tensile Strength of Base Material and HAZ [37]–[39]

Alloy	Ultimate Tensile Strength ksi (MPa)
5083	44.0 (305)
5083 – HAZ	39.2 (270)
6061	38.0 (260)
6061 – HAZ	23.9 (165)

With the maximum loads that the specimen was expected to see determined, the final specimen design was determined. The grip system transferred the load to the specimen by bolts in shear. To design the specimen, four specific limit states were checked:

1. Bolt shear rupture
2. Bolt bearing (tear out)
3. Block shear rupture
4. Net section fracture

Figure 8 illustrates the overall dimensions of the specimen along with the dimensions associated with the bolt pattern. Eight 5/8" bolts arranged in two rows are included in the design to assure that the bolts do not rupture in shear when loaded at the estimated breaking load. The grip section was both lengthened and widened until the specimen surpassed the bearing strength and net section requirements discussed in the previous section. To ensure that the radius of the fillet was not too abrupt, a double-row bolt pattern was selected so that the width of the grip section could be reduced while satisfying the prescribed net section requirement. Overall, the minimum safety factor achieved by the grip section was 1.3, which was deemed adequate for the specimen.

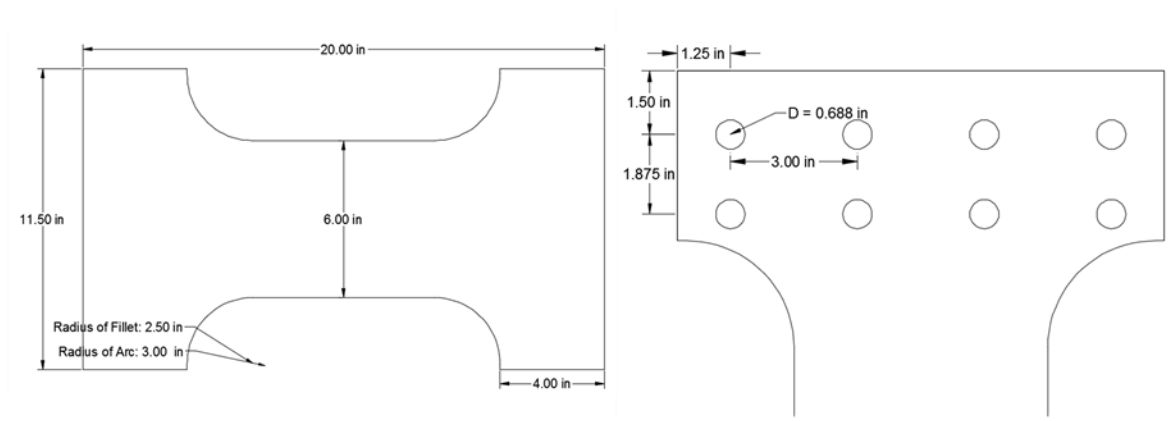

Figure 8: Overall dimensions of the non-load carrying fillet welded connection along with the edge and spacing distances for the proposed bolt pattern.

3.2 Design of Material Characterizations Coupons

The material coupons were designed to follow the ASTM E8 and 0.50 inch wide sheet-type specimens shown in Figure 7. The breaking load of these specimens was estimated at 6-7 kips. Two major types of specimens were required:

1. Standard material specimens, testing the raw plate used to fabricate the larger experimental pieces. Because aluminum often exhibits pronounced anisotropic behavior related to either the work-hardening direction for 5000-series alloys or the direction of extrusion for 6000-series alloys, tests at different orientations are required. In this work, three orientations were selected: 0, 45, and 90 degrees with respect to either the rolling or extrusion direction of the plate. At each direction, five replicate coupons would be cut to study the spatial repeatability of the alloy.
2. Simulated HAZ specimens. Understanding material properties within the HAZ is difficult. In this region, the material properties can change quickly over small length scales. It is possible to use very small-scale coupons extracted from the HAZ by micro-machining [28]. Another system is to simulate a HAZ region by laying down two parallel welds and removing a specimen from the middle region between the welds where a consistent HAZ region will have formed [40], [41]. In this work, an experimental approach was taken, where the weld lines were varied between 1in (25mm), 1.5in (37.5mm), 2in (50mm), 3in (76mm), and 4in (102mm) spacing, and both a hardness specimen and a tensile specimen taken from the region between the welds. It was hoped that this would allow a correlation between the hardness value and specific tensile properties.

3.3 Design of Hardness Coupons

The hardness test specimens were simple rectangles cut to fit the sample space on the Clark Micro-hardness tester used. Specimens were cut 25mm/1” wide with 75mm/3” of length, centered along the weld line. Additional hardness test specimens were cut from the simulated HAZ regions: these specimens were also 25mm/1” wide, but their length was equal to the width of each simulated HAZ.

3.4 Design of Fabrication Procedure

With the specimen design complete, a simple and practical way of manufacturing the specimens was needed. After several iterations, a simple square specimen design was established, consisting of a large square of plate material with a flat bar welded across the material towards one end. The flat bar, and its connection to the plate, provided the HAZ and joint for the NLCFWC, while the remainder of the plate provided room for the material coupon specimens and simulated HAZ specimens. Cross-weld hardness coupons alternated with the NLCFWC. Each square plate was configured to produce three NLCFWC, allowing each larger square plate to cover one alloy and one weld type. Five material hardness coupons were configured per plate at random orientations, allowing three plates in each alloy series to cover the entire material testing requirements. Thus, six plates were needed in the end:

- One plate with a 5000-series alloy, and 3/16” (4.8mm) continuous fillet weld
- One plate with a 5000-series alloy, and 5/16” (7.9mm) continuous fillet weld
- One plate with a 5000-series alloy, and 3/16” (4.8mm) chain fillet weld

- One plate with a 6000-series alloy, and 3/16" (4.8mm) continuous fillet weld
- One plate with a 6000-series alloy, and 5/16" (7.9mm) continuous fillet weld
- One plate with a 6000-series alloy, and 3/16" (4.8mm) chain fillet weld

A sketch showing a plan and side view profile of a sample plate is shown in Figure 9 and Figure 10. The goal of the project was to reflect standard shipyard practice, so the weld procedure was left up to the fabricating yard. Details of the machine settings and procedure used are given in the results section.

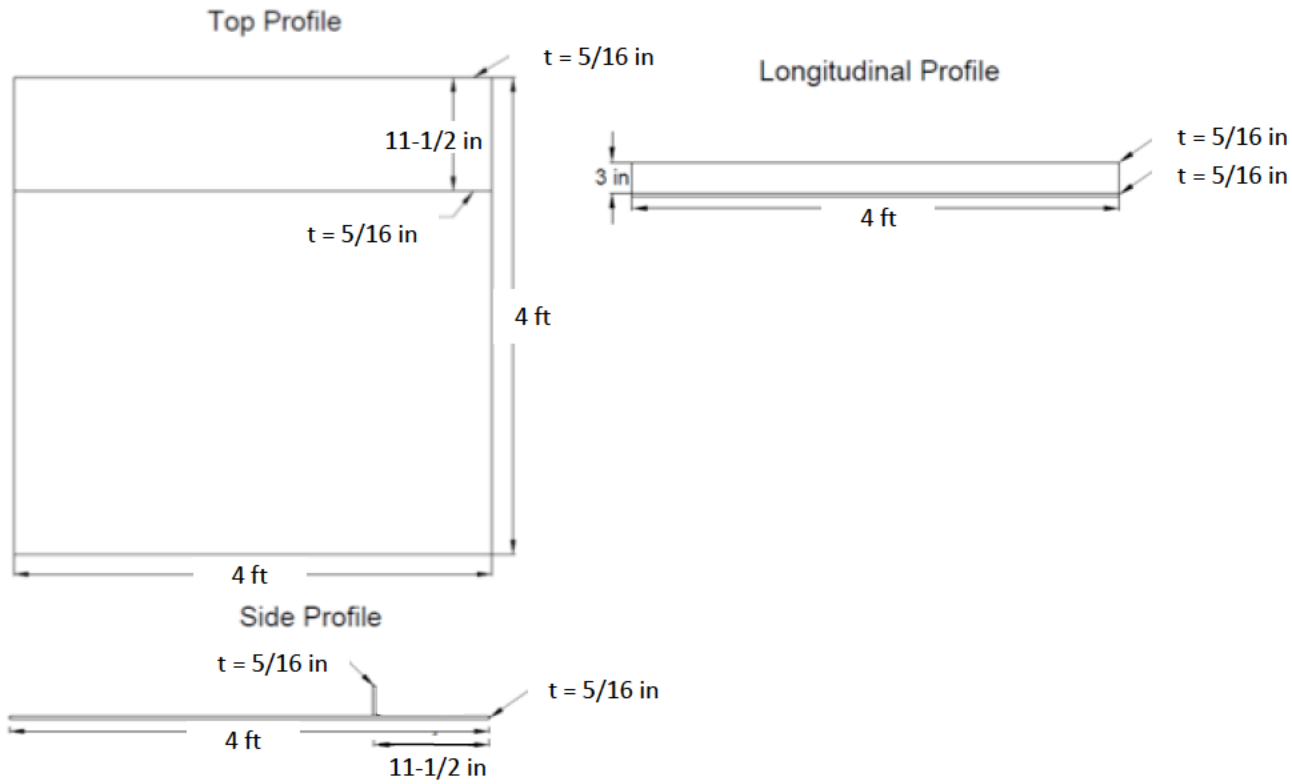

Figure 9: Overall square specimen configuration, showing fillet-welded flat bar 11.5" (292mm) from the end. 5/16" (7.9mm) continuous weld version is shown.

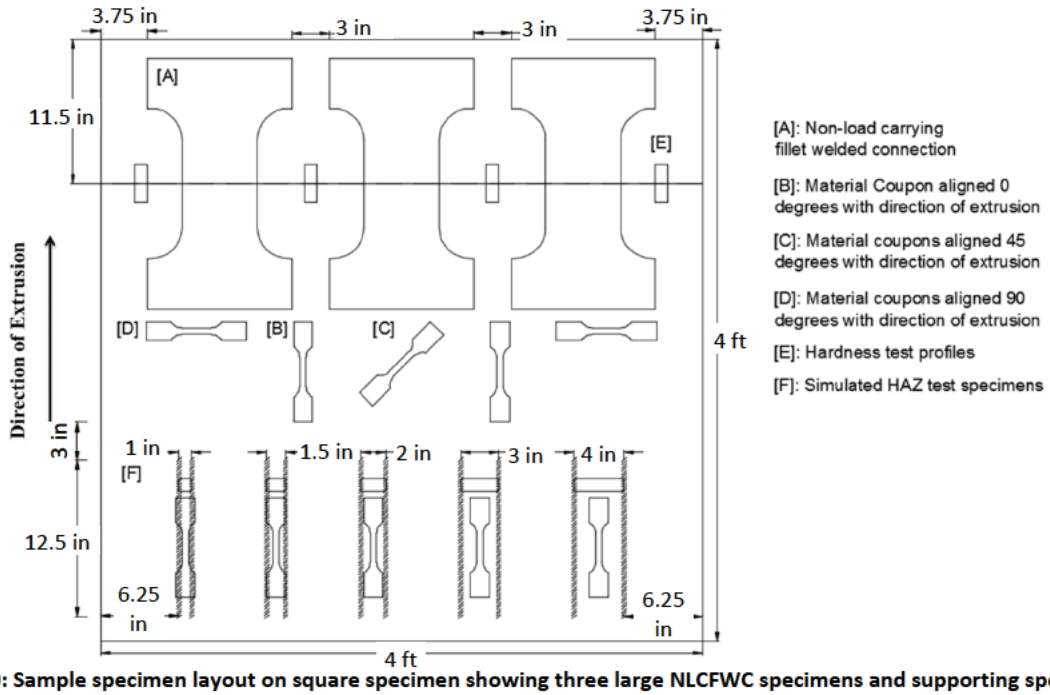

Figure 10: Sample specimen layout on square specimen showing three large NLCFWC specimens and supporting specimens. Note that the distribution of specimen types B, C, D vary plate-to-plate to produce five specimens of each type.

3.5 Development of Complex Cross-Weld Specimens

Two additional more complex specimens were designed as final validation specimens. The first of these simulated a full stiffener/frame intersection location, where in addition to the NLCFWC attaching the frame to the plate, a longitudinal stiffener continue through the connection providing both additional HAZ and some additional continuous material. A mixed-material model was chosen for this connection, reflecting common practice where 5000-series alloys are used for shell plates, but internal stiffeners are often extruded 6000-series shapes. A rendering of this specimen, and fabrication drawings are shown in Figure 11. A 2" (50mm) flat bar was used to simulate the stiffener, and it intersected with the same flat bar used to simulate the transverse frame in the NLCFWC. From this overall specimen, a dog-bone specimen, following the same dimensions as the NLCFWC and re-using the same grips, was fabricated.

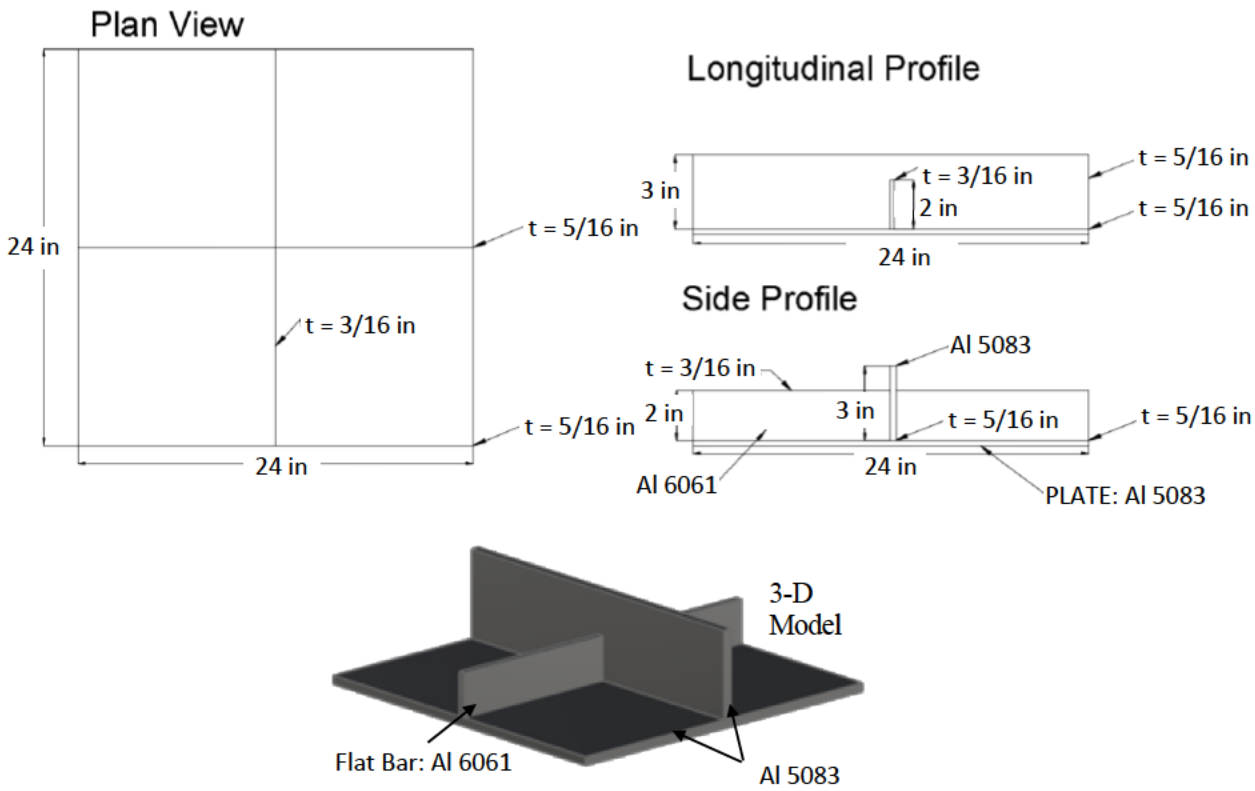

Figure 11: Stiffener/Frame Intersection Specimen

One additional type of joint was also tested to simulate a load-carrying offset fillet weld connection. This type of connection is frequently used when hollow-core 6000-series extrusions must end on a watertight bulkhead or similar member. Normally, in this situation, the top and bottom face sheets of the extrusion are joined to the overall structure via a single-sided fillet weld. Additionally, the location of the welds on the top and bottom face sheets may be offset from each other, meaning that each weld may undergo significant local bending as it is an offset, single-sided joint.

Replicating this type of connection in a small-scale laboratory setting is difficult. Fabricating and testing a specimen with a double-sided extrusion would result in a very large specimen as such extrusions tend to be used for major structural members such as heavy vehicle decks. However, similar HAZ patterns and loading physics can be replicated in a smaller specimen. In the approach taken here, an extruded "T" stiffener was used to stand in for the bulkhead or connecting structural member. Two sheets of 6000-series material were then joined to the T stiffener. Each sheet was placed on top of the flange of the T so that the end of the plate could be joined to the web of the T by a single fillet weld. Then, the specimen was flipped over, and a second fillet weld was added to the end of the flange of the T, where it forms a lap joint with each sheet of 6000-series material. This specimen is shown in Figure 12. In this manner, the load applied to the 6000-series sheets must pass through the two offset, single-sided fillet weld

to transfer into the T stiffener and then back into the second sheet of 6000-series material. Additionally, a complex interaction between the HAZ regions of the two fillet welds is achieved. This covers much of the type of response expected for the hollow-core extrusion joint in a small and compact specimen.

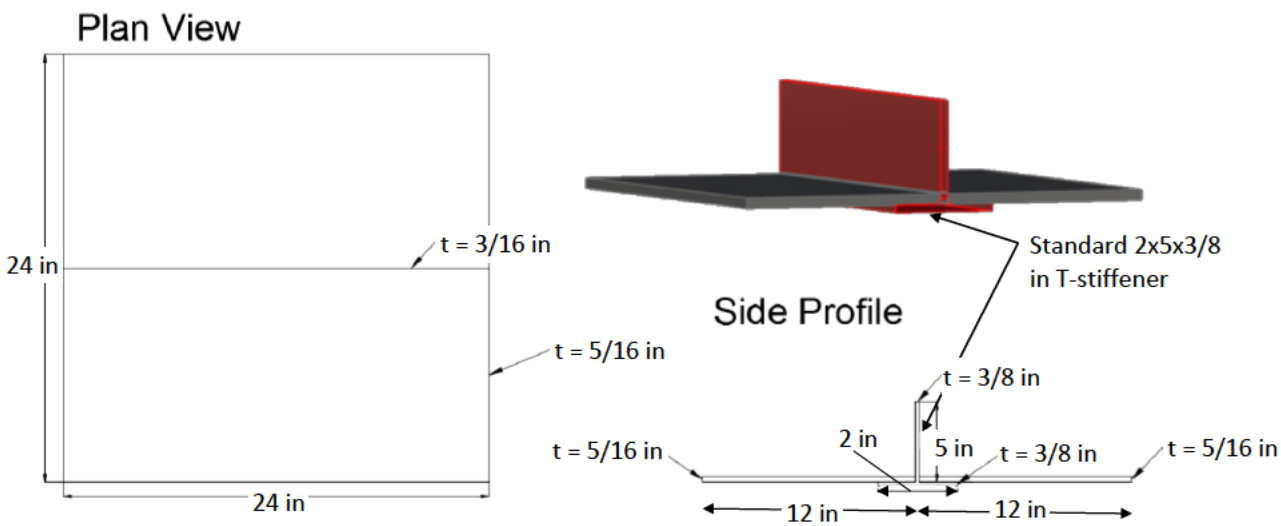

Figure 12: Offset Load-Carrying Fillet Weld Connections Fillet welds were made where the plate intersects the T-stiffener web on the top and where the plate and flange overlap on the bottom

3.6 FEA Validation of NLCFWC

A nonlinear finite element model was created for the 5086 and 6061 NLCFWCs using Abaqus FEA to ensure that the stress concentrations along the fillet and around the bolt holes did not exceed the tensile strength of the base material. Typically, designing tensile specimens within ASTM standards ensures that there should be little to no concern regarding high-stress concentrations along the fillet. However, as the NLCFWC dimensions are not within ASTM standards for plate-type specimens, a finite element model was created and subsequently used to simulate a tensile test to make certain that the NLCFWC fails in the reduced section as intended.

Within Abaqus, a two-dimensional planar (x-y plane) model was created, with the x-axis running perpendicular to the applied loading and the y axis running parallel to the applied loading. As it was assumed that there was no stress or strain in the z-direction since the thickness of the NLCFWC was only 5/16 inches (roughly 8 millimeters). Next, elastic and density properties were defined for the 5086 and 6061 alloys, using the Ramberg Osgood relationship with typical, not grade minimum values.

Only half of the specimen was modeled as an identical response is assumed to occur at the opposite end due to the symmetry of the design. Additionally, the set that defined the top edge of the finite-element model section was subjected to a fixed boundary condition where no

rotations were allowed in the x or z directions, and no displacements were permitted in the y-direction. Next, to simulate a tensile test, three nodes were defined along the bottom of each bolt hole where a displacement was applied. Greater discretization was used when creating the mesh around the fillets and bolt holes to accurately capture the resultant stresses as the specimen was being displaced.

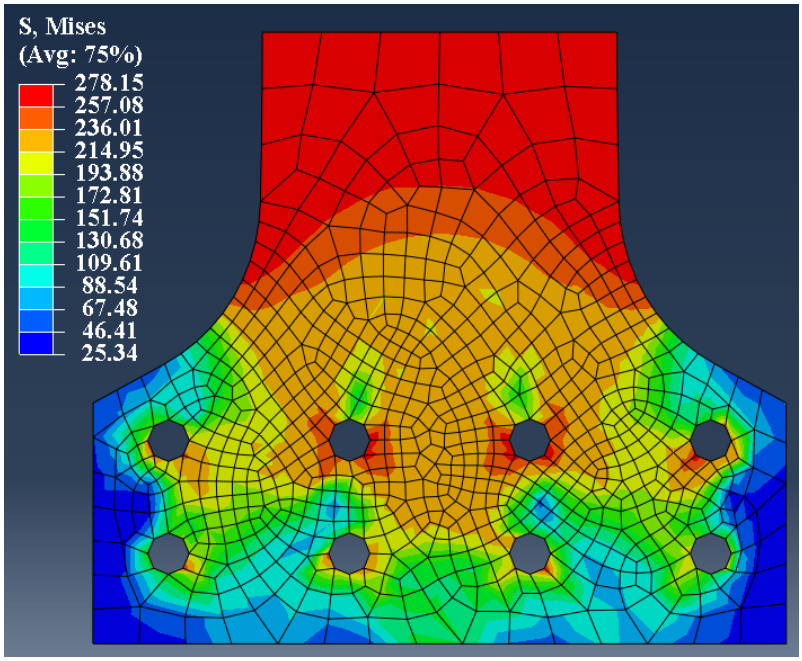

Figure 13: FEA Simulation of Failure

The specimen was then displaced until the estimated ultimate tensile strength of the HAZ was observed along the reduced section. Figure 13 shows the resulting Von Mises stresses throughout the entire specimen. Note that all stresses recorded in the legend have units of MPa. Based on this figure, it is apparent that the stress at the reduced section is approximately 278.1 MPa which correlates to the estimated ultimate tensile strength of 281 MPa for the chain-intermittent fillet weld case. Figure 13 may suggest that the two center bolt holes along the top row exhibit excessive stress concentrations; however, the stresses displayed in these regions are less than the ultimate tensile stress of the 5083 base material.

3.7 Experimental Validation of a Single NLCFWC

To further validate the NLCFWC design before fabricating the final specimens, a full-scale version of the specimen was cut from a plain sheet of 6061-T6 material. This specimen did not feature any weld of the HAZ region, and thus the breaking load of the specimen was expected to be larger than those with HAZ during the experimental program. By testing the unwelded specimen, the grip and overall specimen design could be quickly validated at an even higher breaking load than that expected during the full-scale test. This also gave an opportunity to validate the data acquisition systems planned for use during the test, as well as to provide a dry run with the machine running with a large specimen.

An image of the specimen after failure is shown in Figure 14, along with the digital image correlation system (DIC) used for the test. The specimen fractured smoothly in the middle of the specimen without excessive deformation at the grips or bolts. Based on this successful test, the order was placed to fabricate the full series of NLCFWC specimens as well as the two complex specimens.

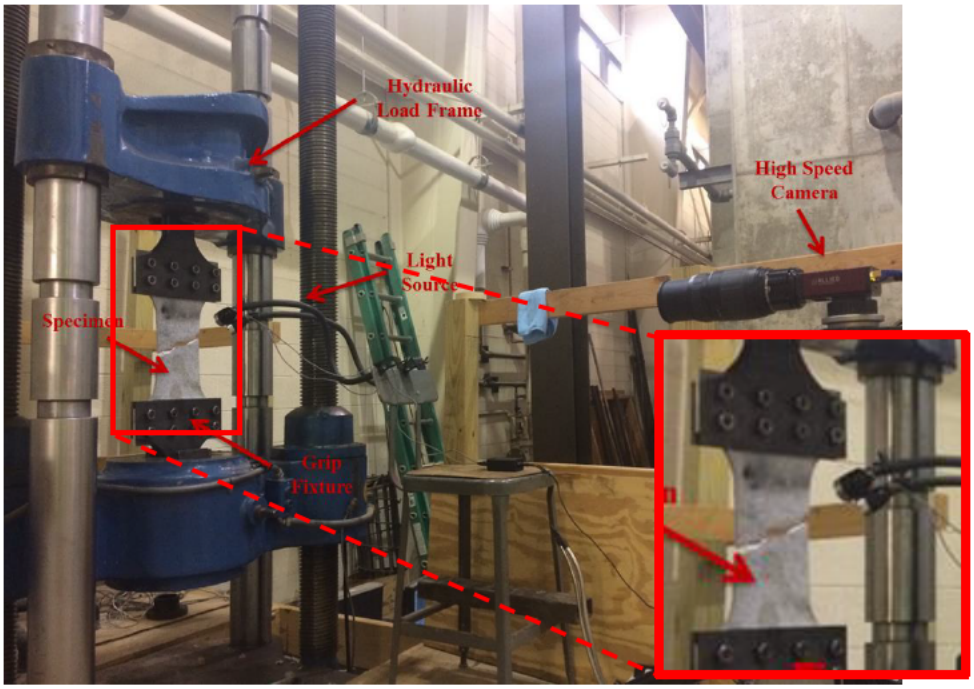

Figure 14: Unwelded Specimen Test Piece After Failure showing DIC Gear Setup

4 Specimen Fabrication and Test Procedure

4.1 Fabrication and Material Certifications

Metal Shark, an experienced aluminum shipbuilder, was selected to provide the fabricated specimens. Metal Shark has built a wide variety of commercial and governmental vessels in aluminum and had previously assisted in fabricating specimens for academic research at Webb Institute. As part of Metal Shark's outreach and education activities, they were willing to provide the specimen at no cost to the research program. Based on material availability, the final alloys selected for fabrication were 5086-H116 and 6061-T651.

The 5086-H116 material was produced by Hulamin in South Africa. The material was rolled in 5/16" (7.9mm) thickness and produced in sheets measuring 60" x 240" (1524mm x 8636mm). The material was Hulamin load number HL019349, lot number 23/12/046D7. The material was produced under ASTM standard B928 for the 5086-H116 temper as well as the American Bureau of Shipping Rules, Part 2, Chapter 5, Section 1. However, a Classification Certificate was not included in the material order for this group. Chemical and material property testing was

provided by Hulamin, with the results as listed in Table 3 and Table 4. The mechanical properties are significantly above those required for 5086-H116 in ASTM B928, and indeed, could be certified as 5083-H116 based on the material properties and chemical composition.

Table 3: Chemical Composition of 5086-H116 Alloy reported by Hulamin, remainder is AL

Si (%)	Fe (%)	Cu (%)	Mn (%)	Mg (%)	Cr (%)	Zn (%)	Ti (%)	Pb (%)	Bi(%)
0.21	0.24	0.05	0.52	4.43	0.12	0.01	0.01	0.00	0.00

Table 4: Mechanical Properties of 5086-H116 Alloy report by Hulamin

Specimen	Yield Strength – ksi (MPa)	UTS – ksi (MPa)	Elongation A50 - %
1	36.4 (251)	49.2 (339)	15
2	36.4 (251)	49.2 (339)	14
3	36.0 (248)	49.2 (339)	15
4	35.2 (243)	49.0 (338)	15
5	35.7 (246)	49.0 (338)	14

The 6061-T651 was produced in China by Henan Mingtai Aluminum Industrial Company, Ltd to ASTM B209-10, ASME SB-209, AMS 4027N, AMS-QQ-A-250/11. The heat number was Z-1510Y6062. The certified chemical properties and mechanical properties from the mill certificate are listed in Table 5 and Table 6. Similar to the 5086-H116 alloy, this particular lot of 6061-T651 is significantly stronger than the grade minimums. At the time of production, the 2010 edition of ASTM B209 was in effect, and this standard only required a yield strength of 35 ksi (241 MPa) and a UTS of 42 ksi (290 MPa).

Table 5: Chemical Composition of 6061-T651 Alloy reported by Henan Mingtai Aluminum, remainder is AL

Si (%)	Fe (%)	Cu (%)	Mn (%)	Mg (%)	Cr (%)	Zn (%)	Ti (%)	Others (%)
0.637	0.325	0.276	0.019	1.109	0.217	0.005	0.022	0.15

Table 6: Mechanical Properties of 6061-T651 Alloy report by Henan Mingtai Aluminum

Specimen	Yield Strength – ksi (MPa)	UTS – ksi (MPa)	Elongation - %
1	41.8 (288)	48.5 (335)	18

The square specimens were fabricated by Metal Shark using the weld parameters listed below:

- Welds with a 3/16” size (4.8mm) were welded at 21 volts, 145 amperes, and 15 inches/minute (381 mm/minute) travel speed
- Welds with a 5/16” size (7.9mm) were welded at 21.8 volts, 157 amperes, and 16 inches/minute (406 mm/minute) travel speed

The 5556 filler alloy was used for all welds.

After receipt and checking of the specimens at the University of Michigan, the specimens were transported to a local machine shop. A waterjet cutting table was used to machine out the specimens following the general layout shown in Figure 10, with a different configuration of material coupons on each sheet to provide specimens at different orientations to the rolling or

extrusion direction of the sheet. Similar specimens were cut for the two larger stiffener and extrusion specimens.

The material at the bottom of one sheet of 5086 and one sheet of 6061 was used to generate simulated HAZ specimens, as shown at the bottom of Figure 10. The goal of this step was to produce material property coupons with uniform heat-impacted properties. To achieve uniform heat reduction, two parallel gas tungsten arc welding (GTAW) passes were made with a GTAW welding machine at the University of Michigan. The distance between these GTAW passes was varied between 25mm and 100mm (1”-4”), with the closer distances producing higher levels of heat impact. No filler metal was used during this procedure; only the arc was struck to the aluminum and then moved along at a normal welding speed. Standard tensile coupons were then machined out of the remaining plate.

4.2 Final Specimen Configurations

After the waterjet cutting of the specimens, the following smaller test specimen matrix was created to track the replicated tests:

Table 7: Final Specimen Numbering by Material and Weld Type

Alloy	**Fillet Weld Size**	**Specimen Number**		
		1	**2**	**3**
5086	4.8mm (3/16”) continuous	A1	A2	A3
5086	4.8mm (3/16”) chain	B1	B2	B3
5086	7.9mm (5/16”) continuous	C1	C2	C3
6061	4.8mm (3/16”) continuous	D1	D2	D3
6061	4.8mm (3/16”) chain	E1	E2	E3
6061	7.9mm (5/16”) continuous	F1	F2	F3

4.3 Material Coupon Testing

Material testing was conducted on an MTS 810 testing system equipped with a 98 kN load cell. A 1”/25mm gauge length was used to record strain.

Figure 15: MTS 810 Machine Used for Material Coupon Testing

Material testing was conducted largely as indicated during the test plan. However, one of the 5086-H116 plates was rotated before fabrication in the shipyard, so that the direction of rolling did not match the originally planned direction. This resulted in some of the material specimens not being cut at the expected orientation with respect to the rolling direction. This reduced the number of 0-degree specimens for 5083-H116 to three. However, the resulting material curves were generally in good agreement even with only three samples. The final numbers of specimens available ended up being:

- 5086-H116 at 0 degrees to rolling – 3 specimens
- 5086-H116 at 45 degrees to rolling – 5 specimens
- 5086-H116 at 90 degrees to rolling – 7 specimens
- 6061-T651 at 0 degrees to extrusion – 5 specimens
- 6061-T651 at 45 degrees to extrusion – 5 specimens
- 6061-T651 at 90 degrees to extrusion – 5 specimens
- Simulated HAZ specimens, 0 degrees to rolling – 5086-H116 – 5 specimens
- Simulated HAZ specimens, 0 degrees to extrusion – 6061-T651 – 5 specimens

4.4 Cross-Weld Hardness Profiles

These specimens were used to track the width of the HAZ for each weld and alloy type, with four replicates per alloy and weld combination. Additionally, a specimen was run for each of the simulated HAZ specimens to try to correlate material stress-strain curves with hardness values. Very little information was available in the literature to develop an experimental procedure for the cross-weld hardness specimen in terms of specimen preparation and the tradeoff between indenter size, force, and accuracy. After trial and error on a few sample specimens, a polishing and testing procedure that yielded consistent results emerged. Each specimen was waterjet cut

out of the material and then ground by 400, 600, and 1200 grit sandpaper followed by 9, 6, 3, and 1 micron polishing solutions. Vickers hardness values were determined via a Clark CM-400AT Micro-hardness tester, using a 300g load and a 10-second indentation time. This machine is in the Van Vlack lab in the Material Science and Engineering department at the University of Michigan. Two hardness lines, each 25mm long, were made on each specimen, starting from the center of the specimen, and working out. As the flat-bar is about 8mm thick, the first 4mm of each hardness profile represents material under the flat bar. A picture of the Clark Micro-hardness tester used is shown in Figure 16.

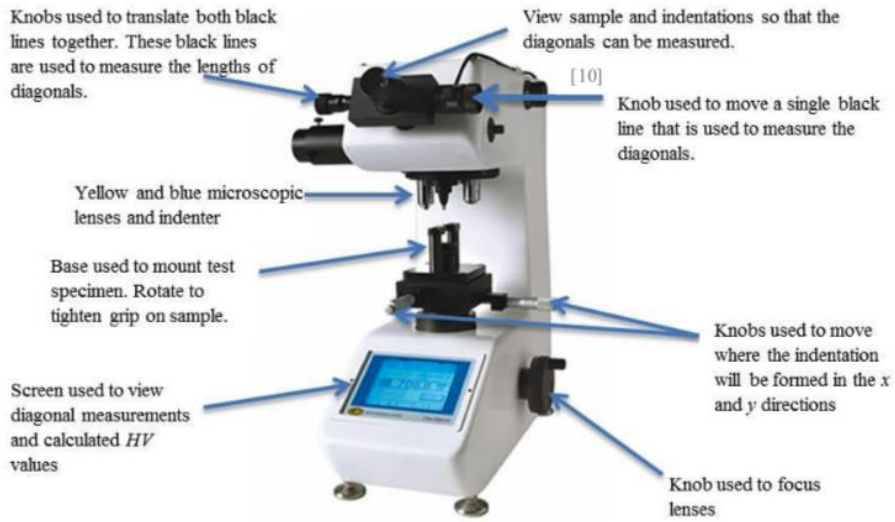

Figure 16: Clark CM-400AT Micro-Hardness Machine used for Weld Hardness Profiles

4.5 NLCFWC and More Complex Connection Experiments

The NLCFWC were tested on a large load frame in the Structural Engineering Laboratory of the Department of Civil and Environmental Engineering at the University of Michigan. This load frame had a capacity in excess of 250 Kips (1112 kN) and could be configured to take the large specimens. A picture of the load frame is shown in Figure 17.

Figure 17: Load Frame for Large Specimen Tests

The following instrumentation used to track the load and response of the specimens:

- The load applied by the load frame was measured by an internal load cell
- The cross-head displacement of the frame was also captured
- The displacement of the specimen was also measured by an independent NDI Optotrak system that tracked several infrared markers applied to the specimen. A series of 16 markers were used on each specimen. 6 markers were placed on each side of the weld HAZ, arranged in a 3 x 2 grid. The grid was set up as follows. The toe position of the fillet weld on each side of the joint was first located, and a line was drawn across the width of the specimen at this point on the opposite side from the weld. Then two parallel lines were drawn, 1” (25mm) and 2” (50mm) offset from this line. A series of three vertical lines were then drawn, one down the central axis of the specimen, and parallel lines 2” (50mm) off-center on each side. This set of 5 lines would create 6 intersections in a 3 x 2 grid, and a single tracking marker was placed on each intersection. The process was then repeated for the second fillet weld, resulting in a total of 12 markers on each specimen. Two further markers were attached to the crosshead of the machine, and two markers were attached to a stationary part of the machine so that the cross-head displacement could be tracked and correlated with the load cell measurement above. An image of a specimen showing the markers located is shown in Figure 18.
- Additionally, digital image correlation (DIC) was used to track the displacement fields on the weld side of the specimen. A Prosilica GX3300 camera was used with a custom lighting solution to image the DIC field. A DIC speckle pattern was applied to each

specimen. After significant experimentation, it was determined that a white speckle pattern on a black background provided the best DIC results with the lighting in the lab.

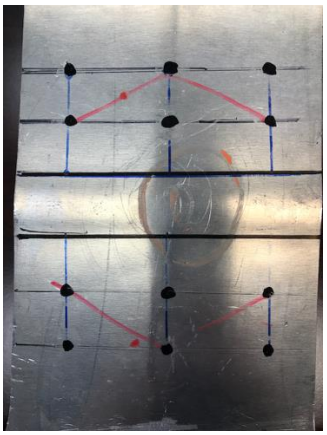

(a) Layout of 3 x 2 sensor grids on each side of the weld

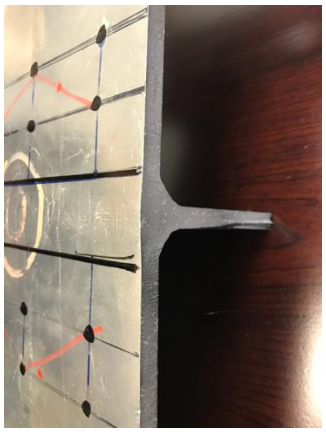

(b) Location of grids with respect to weld toes

(c) Complete specimen mounted with 12 markers on the specimen

Figure 18: Location of Optotrak Markers for Specimen

5 Results

5.1 Base Material Coupons at Different Orientations

The material response is shown in Figure 19 and Figure 20, with the mechanical properties summarized in Table 8 and Table 9. A Ramberg-Osgood stress-strain curve was also fit to the results, following equation (2).

A uniform elastic modulus of 70,000 MPa was assumed, and the mean proof stress listed in Table 8 and Table 9 was used to fit the value of n in the equation. Given the shape of the material curves, especially for the 5086 alloy, this fit was repeated twice for each group of specimens. For the first fit, the entire stress-strain curve until fracture was used to fit, and for the second, the fit was concentrated between strain values of 0% and 1%. This smaller region is often most critical for the initial failure of structures. As seen in the tables, for some directions and alloys, these two fits differed significantly.

As expected for aluminum, there is anisotropic behavior, with softer curves (more pronounced curvature near the proof stress value) at 45° and 90° to the rolling or extruding direction. Within the sheets tested (all sheets of the same alloy were from the same supplier), material property variability was very low. It is important to note that the material provided for this testing was from a single lot for each alloy, and such low material property variability should not be assumed for lot-to-lot variability or variability between materials from different suppliers.

Table 8: Material Coupon Tests, True Stress-Strain Properties

		5086			6061		
		0°	45°	90°	0°	45°	90°
0.2% Offset Proof Stress (MPa)	Min	229	187	148	295	281	281
	Mean	232	195	204	296	284	282
	Max	234	200	217	301	289	283
Ultimate Stress (MPa)	Min	367	340	386	363	344	344
	Mean	373	363	393	367	351	349
	Max	378	380	401	370	359	356
Ultimate strain mm/mm	Min	0.11	0.11	0.16	0.13	.09	0.11
	Mean	0.12	0.17	0.17	0.15	0.13	0.12
	Max	0.13	0.20	0.19	0.17	0.19	0.16
R-O exponent entire curve		8.6	7.1	6.8	19.6	18.8	18.5
R-O exponent fit up to 1% strain		21.4	10.2	7.9	27.9	19.2	20.9

Table 9: Material Coupon Tests, Engineering Stress-Strain Properties

		5086			6061		
		0°	45°	90°	0°	45°	90°
0.2% Offset Proof Stress (MPa)	Min	228	186	146	293	279	279
	Mean	230	194	203	294	282	280
	Max	232	199	215	298	287	281
Ultimate Stress (MPa)	Min	330	299	329	326	314	314
	Mean	332	308	333	328	318	317
	Max	334	313	336	332	320	319
Ultimate strain mm/mm	Min	0.12	0.12	0.17	0.14	0.09	0.11
	Mean	0.13	0.19	0.19	0.16	0.14	0.13
	Max	0.14	0.22	0.21	0.18	0.21	0.17
R-O exponent entire curve		10.9	9.4	8.6	36.0	31.9	30.6
R-O exponent fit up to 1% strain		23.0	10.6	8.1	29.8	20.4	22.4

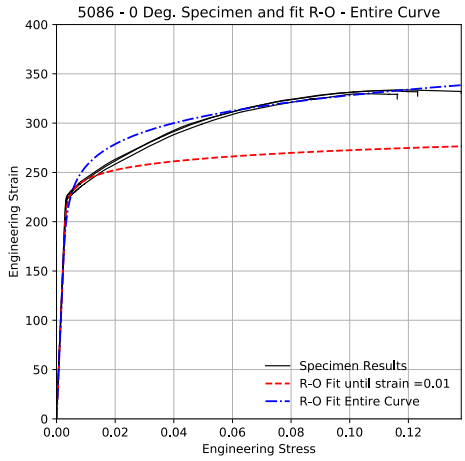

(a)

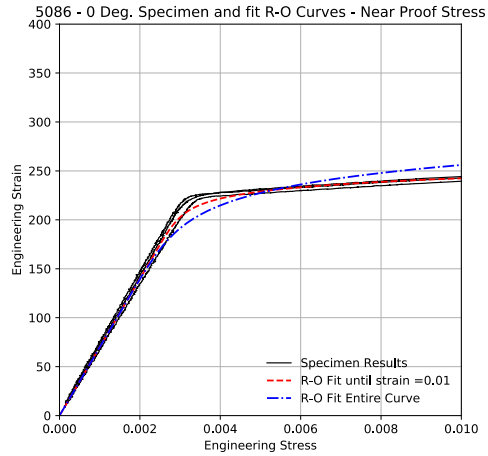

(b)

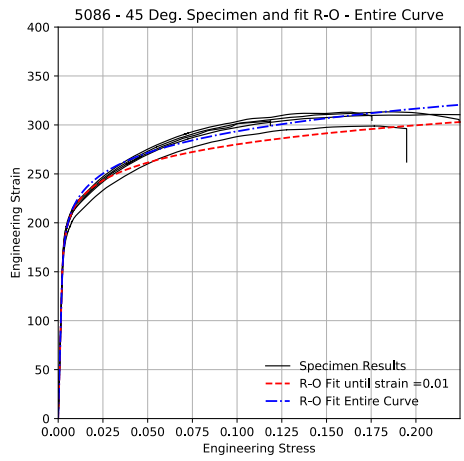

(c)

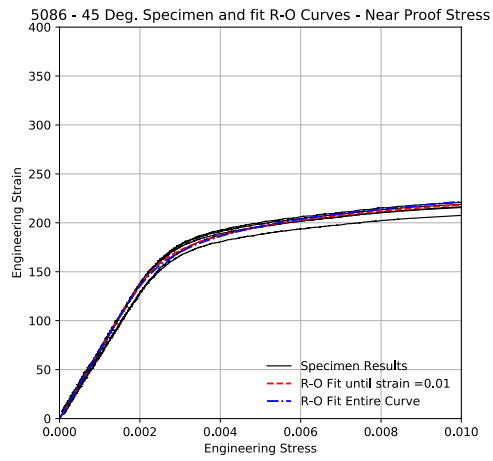

(d)

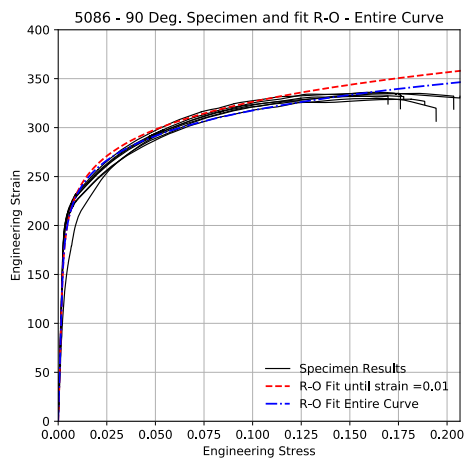

(e)

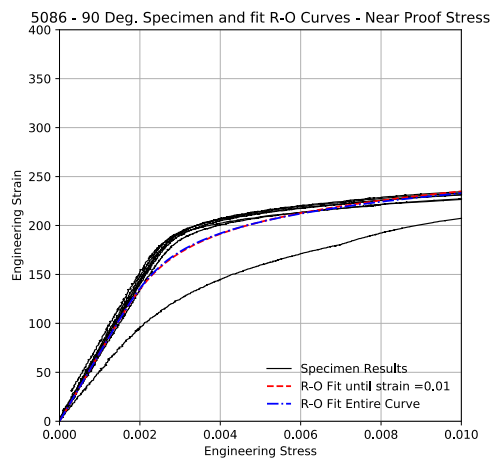

(f)

Figure 19: Engineering Stress-Strain Curves for 5086 Material Coupons with Ramberg-Osgood Fits

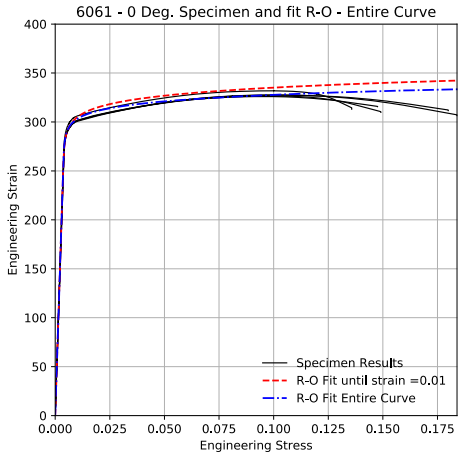

(a)

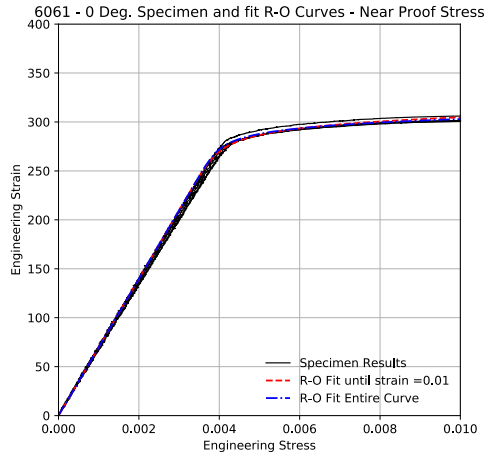

(b)

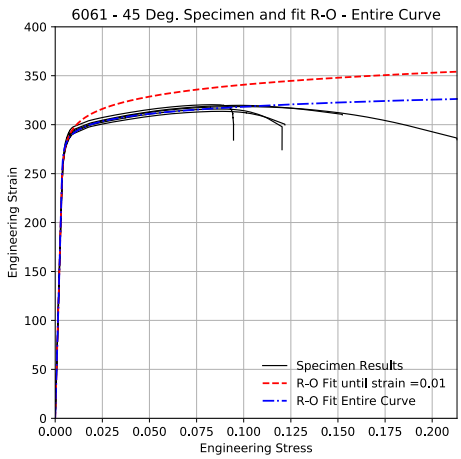

(c)

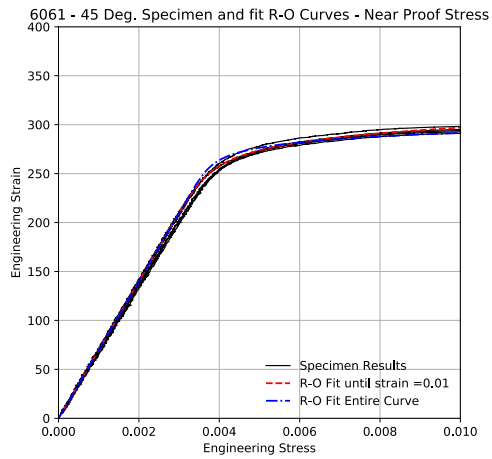

(d)

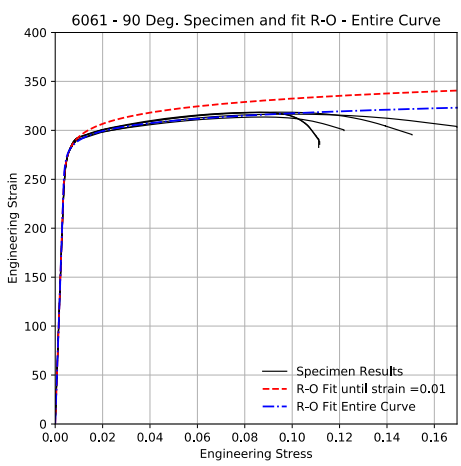

(e)

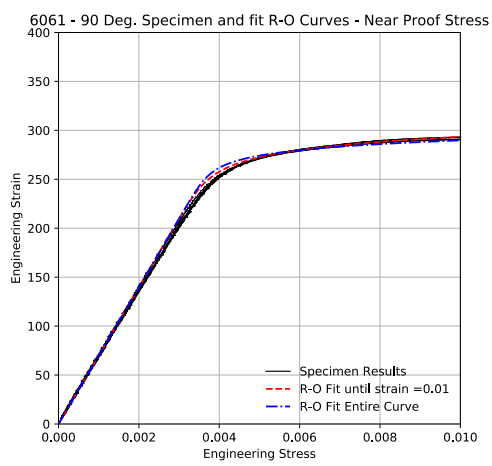

(f)

Figure 20: Engineering Stress-Strain Curves for 6061 Material Coupons with Ramberg-Osgood Fits

5.2 Cross-Weld Hardness and Simulated HAZ

Specimens of type "E" were cross-HAZ hardness specimens. These specimens were used to track the width of the HAZ for each weld and alloy type, with four replicates per alloy and weld combination. Each specimen was waterjet cut out of the material and then ground by 400, 600, and 1200 grit sandpaper followed by 9, 6, 3, and 1 micron polishing solutions. Vickers hardness values were determined via a Van Vlack Micro-hardness tester, using a 300g load and a 10-second indentation time. Two hardness lines, each 25mm long, were made on each specimen, starting from the center of the specimen, and working out. As the flat bar is about 8mm thick, the first 4mm of each hardness profile represents material under the flat bar. The hardness profiles are shown in Figure 21 - Figure 26, where the average of the four specimens is shown in the heavy dashed line, and the individual specimens are shown in the lighter colored lines. These hardness profiles follow what is expected for the alloys; the hardness loss is more pronounced in the 6061 alloy, which follows a "W" pattern indicating some natural aging near the fusion line. The larger welds had larger HAZ, and none of the HAZ are as large as the commonly assumed 1"/25mm standard used in most design codes.

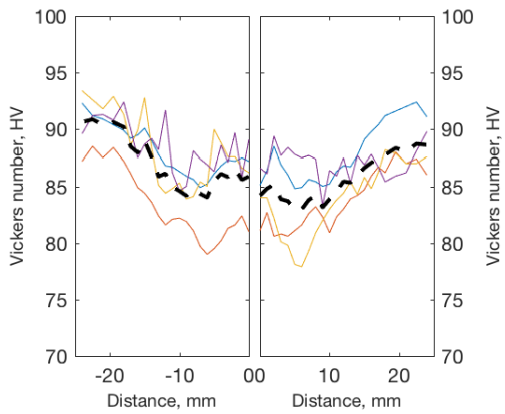

Figure 21: Cross-weld hardness profile of 5086 specimen with 5/16 weld. Heavy dashed line is the average of all four specimens. The center of flat bar is at 0mm distance.

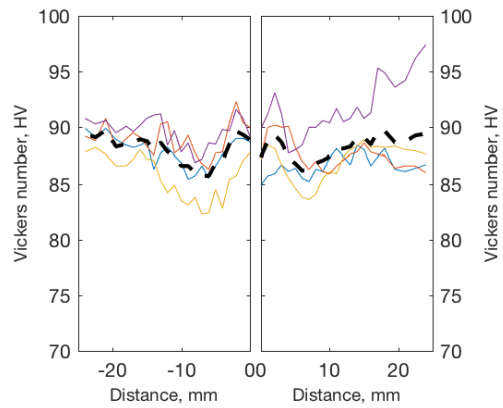

Figure 22: Cross-weld hardness profile of 5086 specimen with 3/16 weld. Heavy dashed line is the average of all four specimens. The center of flat bar is at 0mm distance.

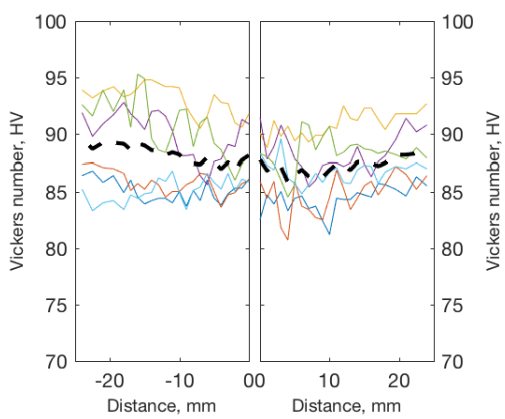

Figure 23: Cross-weld hardness profile of 5086 specimen with chain weld. Heavy dashed line is the average of all four specimens. The center of flat bar is at 0mm distance.

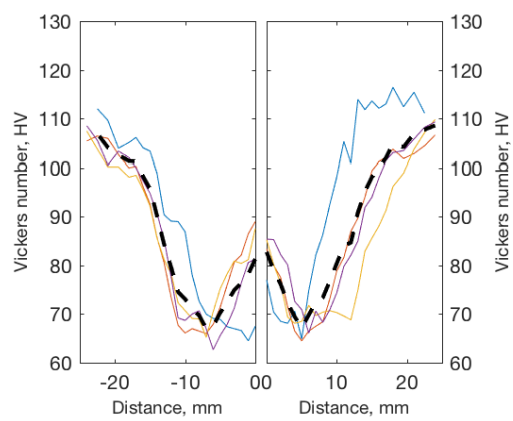

Figure 24: Cross-weld hardness profile of 6061 specimen with 5/16 weld. Heavy dashed line is the average of all four specimens. The center of flat bar is at 0mm distance.

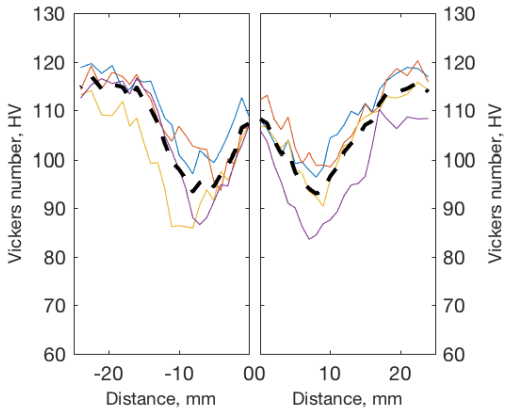

Figure 25: Cross-weld hardness profile of 6061 specimen with 3/16 weld. Heavy dashed line is the average of all four specimens. The center of flat bar is at 0mm distance.

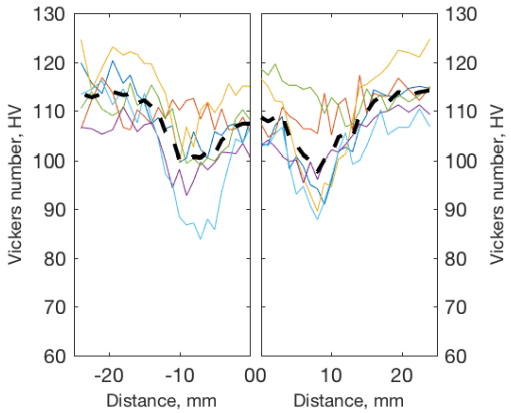

Figure 26: Cross-weld hardness profile of 6061 specimen with chain weld. Heavy dashed line is the average of all four specimens. The center of flat bar is at 0mm distance.

The simulated HAZ specimens (F in Figure 10) were produced on-campus at Michigan. These specimens used autogenous GTAW welding passes without depositing any material to simulate different regions of the HAZ. Two weld passes were made in parallel to create a consistent HAZ region between the parallel passes. Five sets of two parallel weld passes, approximately 400mm/16” long, were made on one plate of each alloy. Then, a hardness coupon and tensile material specimen were machined with their centerlines parallel to the weld passes and in the middle of the two passes. The passes are shown in cross-hatched lines in Figure 10. In this way, consistent thermally impacted material was generated at different levels of heat exposure. The weld spacing was 25mm/1”, 38mm/1.5”, 51mm/2”, 76mm/3”, and 102mm/4” to hopefully generate different HAZ regions. The GTAW setup did not allow capturing of the heat input directly or the welding parameters.

The tensile material properties for these tests are shown in Table 10, as well as Figure 27 and Figure 28. As expected, the 25mm/1” specimens show the largest decrease in strength and hardness. Despite making the passes quite close, the narrow HAZ width observed in the cross-weld hardness profiles appears to also occur in these simulated HAZ specimens. The stress-strain curves quickly recover to the near-base strength value, and little difference can be seen in the 51mm/2” spacing or higher. In the future, higher and more controlled heat input may be necessary when attempting to get a good HAZ simulation with this technique. It is possible the not depositing any weld metal and the loss of the thermal input into the base material as this weld metal solidifies means that the autogenous GTAW passes were not doing a good job of replicating the total amount of heat input into the base material a true weld. This step in the procedure was not well-characterized during the current experiment. Future work could employ thermal sensors or more detailed microstructure evaluations to help quantify the best way to replicate HAZ material. Alternatively, smaller tensile specimens, such as those used by Matusiak [11], could be directly cut from additional weld cross-section profiles.

Table 10: Simulated HAZ Material Properties

Alloy	Weld Spacing (mm/in)	Hardness, HV	Proof Stress (MPa)	UTS Stress (MPa)
5086	25mm/1in	89.4	209	334
5086	38mm/1.5in	90.5	224	338
5086	51mm/2in	92.4	230	340
5086	76mm/3in	93.6	224	338
5086	102mm/4in	93.8	232	341
6061	25mm/1in	99.2	272	305
6061	38mm/1.5in	108.7	296	331
6061	51mm/2in	111.0	298	333
6061	76mm/3in	109.9	296	332
6061	102mm/4in	114.0	298	333

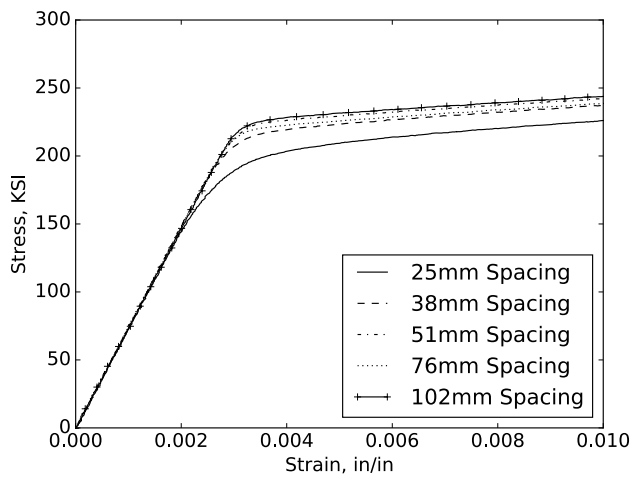

Figure 27: HAZ Tensile Coupons of 5086 Plate

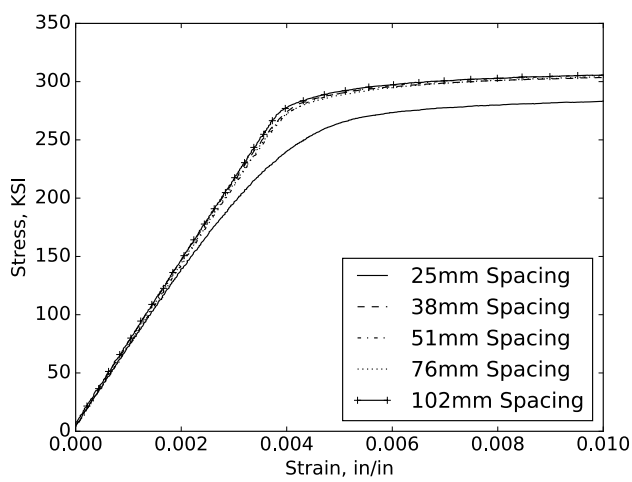

Figure 28: HAZ Tensile Coupons of 6061 Plate

5.3 NLCFWC Specimens

The breaking load of each specimen is given in Table 11. The specimens revealed several interesting trends. Foremost, like the material properties, the breaking load is relatively consistent for each weld configuration, with a variation on the order of 5%. Each specimen was manufactured from the same welding pass, so the full variability of the welder on the connection is not included in this study. However, the consistency is still remarkable. The final failure occurred with a ductile fracture running at 45 degrees in all cases. The fracture started in the HAZ at the toe of the fillet weld and could run into the plate or back under the stiffener. Pre and Post failure pictures for each specimen are shown in the sections below. Notably, the amount of welding certainly has an impact on the 6061 specimens, with a noticeable reduction in the breaking load for the 7.9mm fillet weld size compared to the 4.8mm weld size.

Table 11: Final Breaking Loads in kN

Specimen Letter	**Specimen Number**		
	1	**2**	**3**
A 5086 4.8mm Cont.	402	406	389*
B 5086 4.8mm Broken	400	399	391*
C 5086 7.9mm Cont.	391	388	390
D 6061 4.8mm Cont.	355	359	357
E 6061 4.8mm Broken	370	372	372
F 6061 7.9mm Cont.	303	302	288

*Indicate a specimen that broke in the grips instead of the test section.

While crosshead displacement and Opti track markers were used to measure the displacement, many of the displacement curves had unusual features at lower stress values. Averaged curves across several markers are presented in section 5.2 below in comparison with the finite element results, but individual curves are not presented in this section. These curves are under further analysis, and a supplementary report may be issued in the future with more individual specimen results.

5.3.1 Specimen A1

5.3.1.1 Initial Geometry

Figure 29: Specimen A1 Before Testing

5.3.1.2 Load-Extension Behavior

Specimen A1 failed at a load of 402 kN at the weld toe.

5.3.1.3 Post-Failure Pictures

(a) **(b)**

Figure 30: Specimen A1 Showing Failure at Weld Toe

5.3.2 Specimen A2

5.3.2.1 Initial Geometry

Figure 31: Specimen A2 Before Testing

5.3.2.2 Load-Extension Behavior

Specimen A2 failed at a load of 406 kN with a failure at the weld toe.

5.3.2.3 Post-Failure Pictures

(a) **(b)**

Figure 32: Specimen A2 Showing Failure at Weld Toe

5.3.3 Specimen A3

5.3.3.1 Initial Geometry

(a)

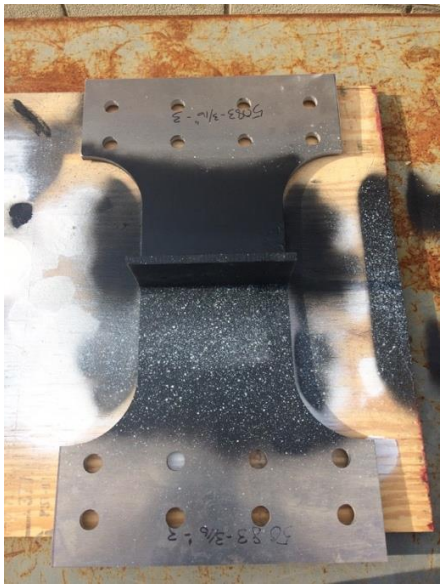

(b)

Figure 33: Specimen A3 Before Testing

5.3.3.2 Load-Extension Behavior

Specimen A3 failed at a load of 389 kN. This specimen failed in the grip section, not at the weld toe. This appeared to be a block shear failure influenced by the stress concentration at the fillet between the reduced width section and the bolting section. This failure mode did not occur on the unwelded test specimen, even though that specimen reached a higher load with the same bolting pattern. It is possible that the difference in aligning the specimens could have resulted in higher loads being carried by the inner two bolts in the first row of this specimen, causing this failure. Using textured steel grips, where the bolts only apply a normal force to drive the grip pattern into the softer aluminum specimen, would be an improvement on the current setup.

5.3.3.3 Post-Failure Pictures

(a) (b)

Figure 34: Specimen A3 Showing Failure at Bolt Holes

5.3.4 Specimen B1

5.3.4.1 Initial Geometry

Figure 35: Specimen B1 Before Testing

5.3.4.2 Load-Extension Behavior

Specimen B1 failed at a load of 400 kN at the weld toe.

5.3.4.3 Post-Failure Pictures

No post-failure pictures were available for this specimen, but the failure mode was identical to other weld toe failures.

5.3.5 Specimen B2

5.3.5.1 Initial Geometry

Figure 36: Specimen B2 Before Testing

5.3.5.2 Load-Extension Behavior

Specimen B2 failed at a load of 399 kN at the weld toe.

5.3.5.3 Post-Failure Pictures

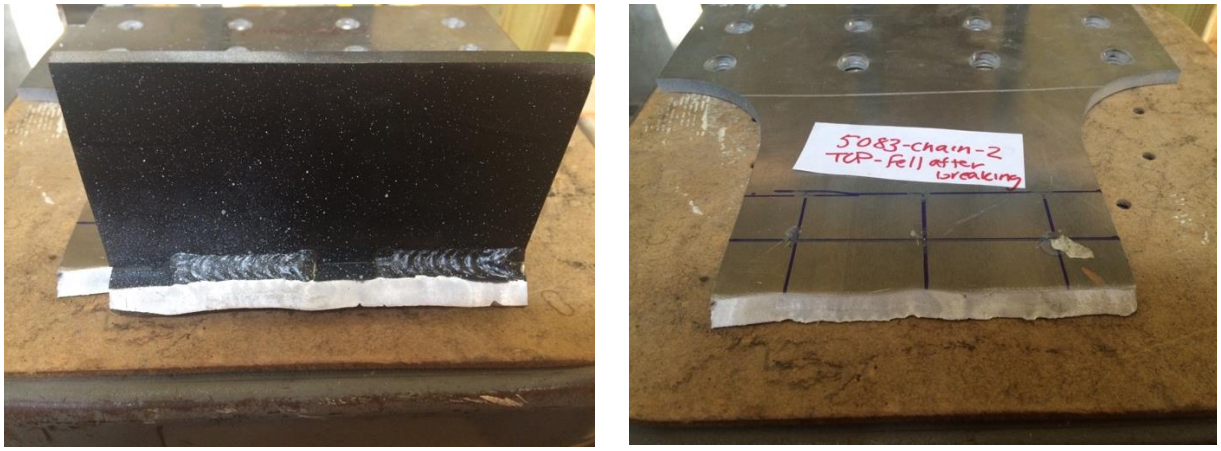

(a) **(b)**

Figure 37: Specimen B2 Showing Failure at Weld Toe

5.3.6 Specimen B3

5.3.6.1 Initial Geometry

Figure 38: Specimen B3 Before Testing

5.3.6.2 Load-Extension Behavior

Specimen B3 failed at a load of 391 kN in the bolting region. The failure was similar to that of specimen A3.

5.3.6.3 Post-Failure Pictures

(a)

(b)

Figure 39: Specimen B3 Showing Failure in Bolting Region

5.3.7 Specimen C1

5.3.7.1 Initial Geometry

Figure 40: Specimen C1 Before Testing

5.3.7.2 Load-Extension Behavior

Specimen C1 failed at a load of 391 kN at the weld toe.

5.3.7.3 Post-Failure Pictures

(a) **(b)**

Figure 41: Specimen C1 Showing Failure at the Weld Toe

5.3.8 Specimen C2

5.3.8.1 Initial Geometry

Figure 42: Specimen C2 Before Testing

5.3.8.2 Load-Extension Behavior

Specimen C2 failed at a load of 388 kN at the weld toe.

5.3.8.3 Post-Failure Pictures

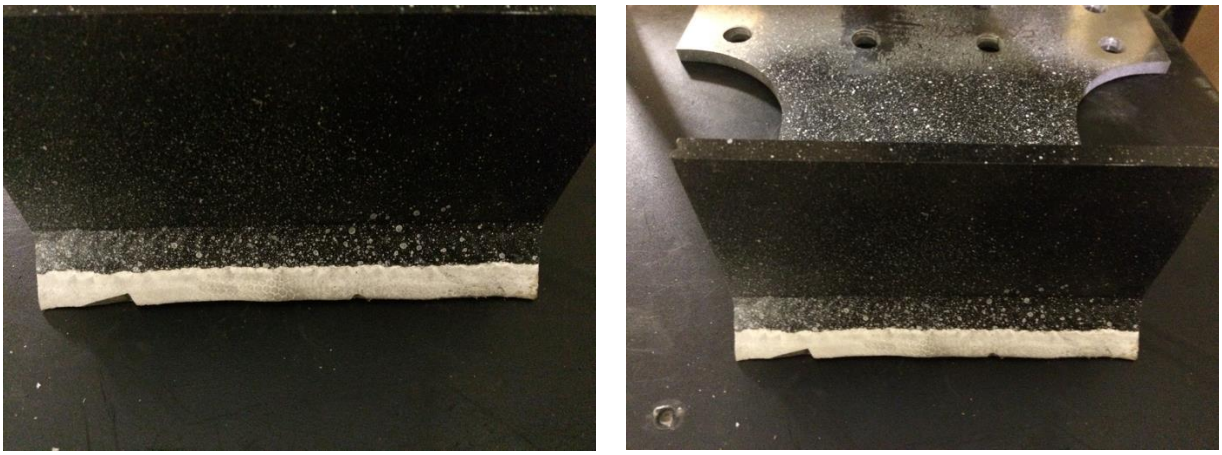

(a) **(b)**

Figure 43: Specimen C2 Showing Failure at the Weld Toe

5.3.9 Specimen C3

5.3.9.1 Initial Geometry

Figure 44: Specimen C3 Before Testing

5.3.9.2 Load-Extension Behavior

Specimen C3 failed at a load of 390 kN at the weld toe.

5.3.9.3 Post-Failure Pictures

(a) **(b)**

Figure 45: Specimen C3 Showing Failure at the Weld Toe

5.3.10 Specimen D1

5.3.10.1 Initial Geometry

No pictures were available of Specimen D1 before failure

5.3.10.2 Load-Extension Behavior

Specimen D1 failed at a load of 355 kN at the weld toe.

5.3.10.3 Post-Failure Pictures

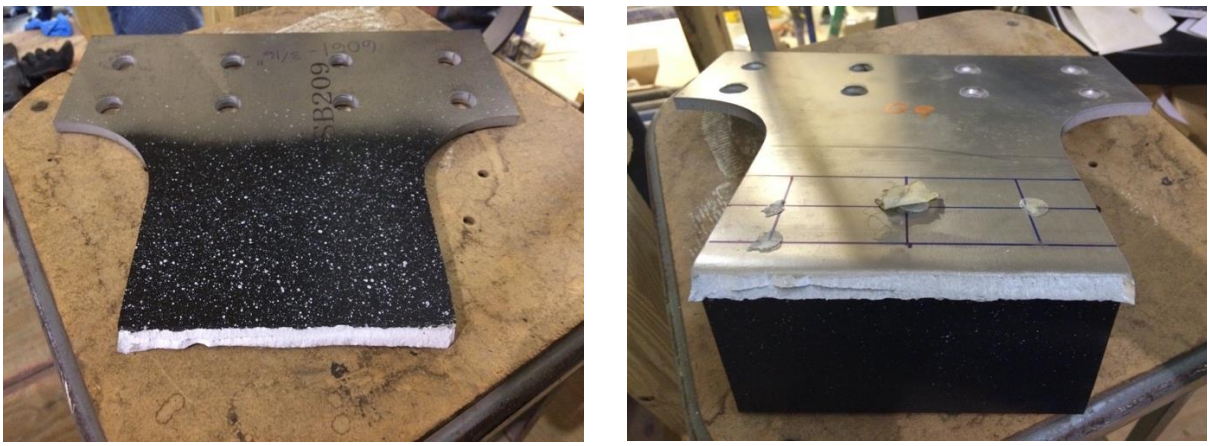

(a) **(b)**

Figure 46: Specimen D1 Showing Failure at the Weld Toe

5.3.11 Specimen D2

5.3.11.1 Initial Geometry

Figure 47: Specimen D2 Before Testing

5.3.11.2 Load-Extension Behavior

Specimen D2 failed at a load of 359 kN at the weld toe.

5.3.11.3 Post-Failure Pictures

Specimen D2 did not have post-failure pictures taken. The failure mode was identical to other weld toe failures.

5.3.12 Specimen D3

5.3.12.1 Initial Geometry

Figure 48: Specimen D3 Before Testing

5.3.12.2 Load-Extension Behavior

Specimen D3 failed at a load of 357 kN at the weld toe.

5.3.12.3 Post-Failure Pictures

(a) **(b)**

Figure 49: Specimen D3 Showing Failure at the Weld Toe

5.3.13 Specimen E1

5.3.13.1 Initial Geometry

Figure 50: Specimen E1 Before Testing

5.3.13.2 Load-Extension Behavior

Specimen E1 failed at a load of 370 kN at the weld toe. The failure surface often reversed directions around the chain welds, as shown in the photos below.

5.3.13.3 Post-Failure Pictures

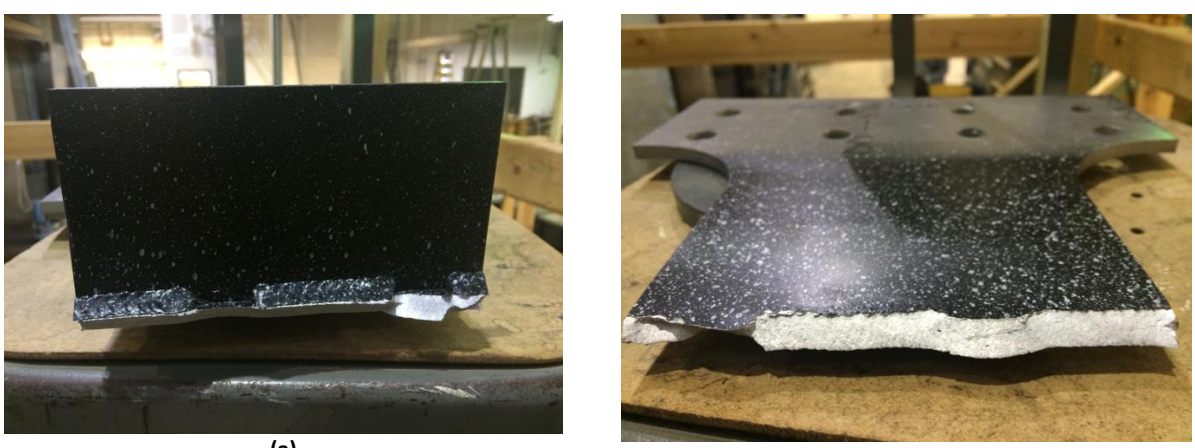

(a) **(b)**

Figure 51: Specimen E1 Showing Failure at the Weld Toe

5.3.14 Specimen E2

5.3.14.1 Initial Geometry

Figure 52: Specimen E2 Before Testing

5.3.14.2 Load-Extension Behavior

Specimen E1 failed at a load of 372 kN at the weld toe. The failure surface often reversed directions around the chain welds, as shown in the photos below.

5.3.14.3 Post-Failure Pictures

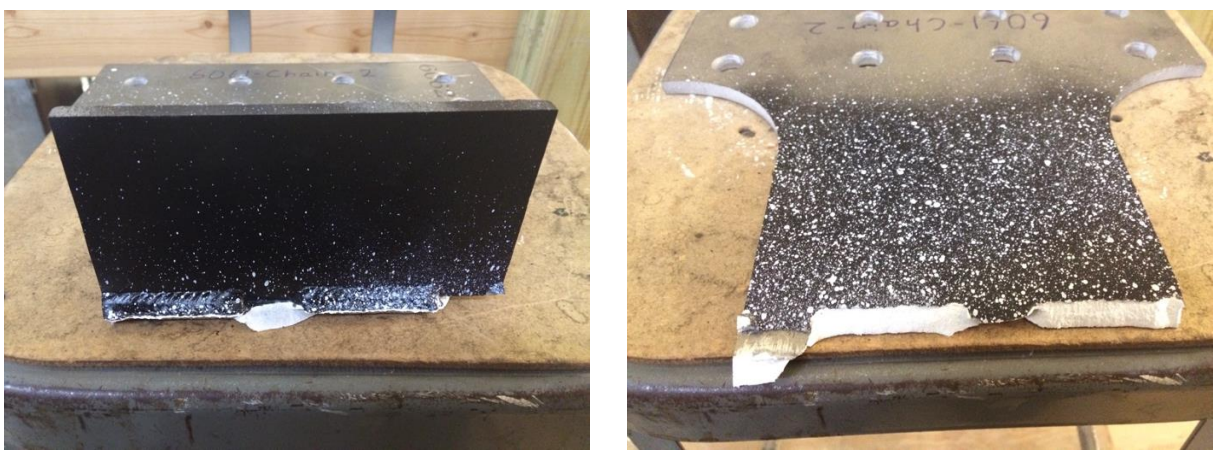

(a) **(b)**

Figure 53: Specimen E2 Showing Failure at the Weld Toe

5.3.15 Specimen E3

5.3.15.1 Initial Geometry

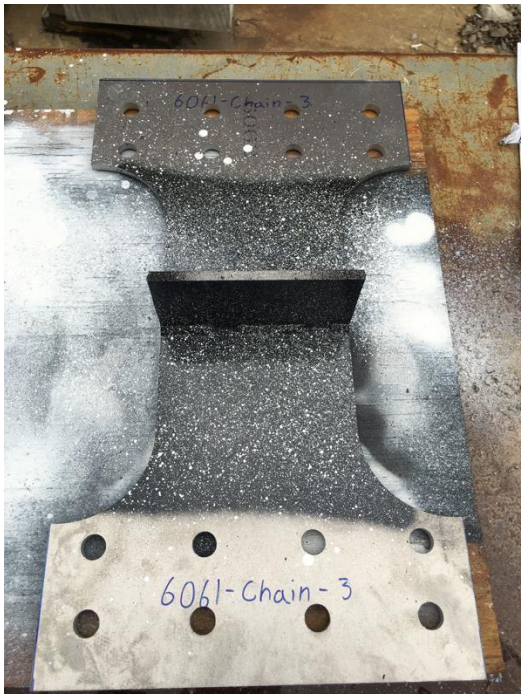

Figure 54: Specimen E3 Before Testing

5.3.15.2 Load-Extension Behavior

Specimen E3 failed at a load of 372 kN at the weld toe. The failure surface often reversed directions around the chain welds, as shown in the photos below.

5.3.15.3 Post-Failure Pictures

(a) **(b)**

Figure 55: Specimen E3 Showing Failure at the Weld Toe

5.3.16 Specimen F1

5.3.16.1 Initial Geometry

Figure 56: Specimen F1 Before Testing

5.3.16.2 Load-Extension Behavior

Specimen F1 failed at a load of 303 kN at the weld toe.

5.3.16.3 Post-Failure Pictures

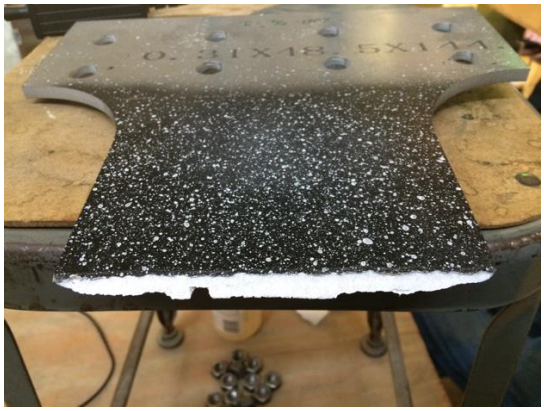

(a)

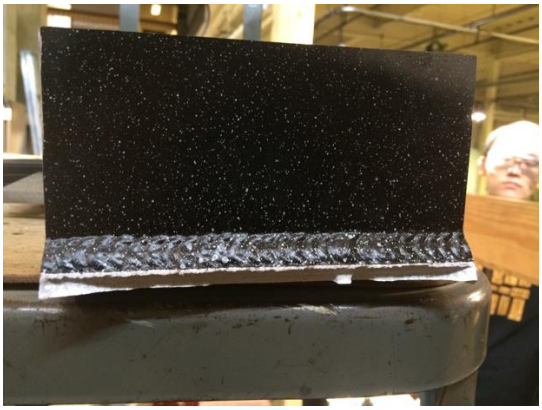

(b)

Figure 57: Specimen F1 Showing Failure at the Weld Toe

5.3.17 Specimen F2

5.3.17.1 Initial Geometry

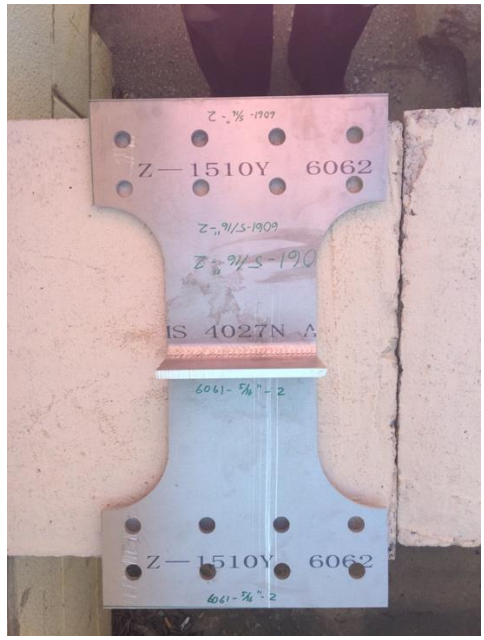

Figure 58: Specimen F2 Before Testing

5.3.17.2 Load-Extension Behavior

Specimen F2 failed at a load of 302 kN at the weld toe.

5.3.17.3 Post-Failure Pictures

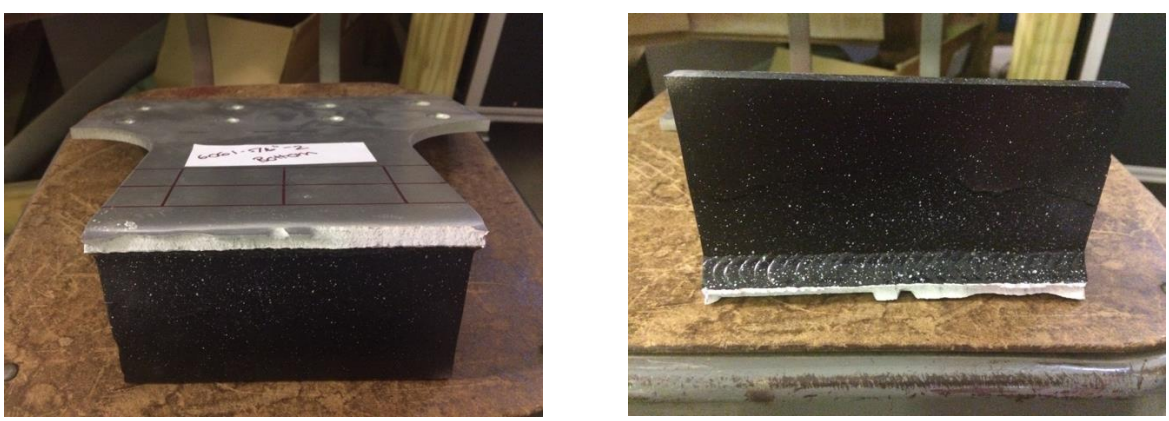

(a) **(b)**

Figure 59: Specimen F2 Showing Failure at the Weld Toe

5.3.18 Specimen F3

5.3.18.1 Initial Geometry

Figure 60: Specimen F3 Before Testing

5.3.18.2 Load-Extension Behavior

Specimen F3 failed at a load of 288 kN at the weld toe.

5.3.18.3 Post-Failure Pictures

(a)

(b)

Figure 61: Specimen F3 Showing Failure at the Weld Toe

6 Comparison with FEA and Design Methods

The ability of engineering models and FEA simulations to model the behavior of undermatched welds is critical in being able to investigate how such connections impact the overall structural performance. Given the different length scales involved, from the narrow undermatched region near welds that is on the order of tens of millimeters to the overall length of the structure, which is often more than 100m in length, a variety of engineering modeling approaches are required. Here, a detailed FEA simulation using solid elements to make a detailed model of the specimen is used. While element fracture criteria were not used in this model (e.g., the final failure of the material and the ductile fracture growth are not included), this model provides an otherwise detailed view of the stress and deflection history of the specimen. For larger models, an abstraction such as a cohesive zone approach may be necessary.

6.1 FEA Simulations

The FEA simulations attempted to model the complete process of the aluminum test. A multi-component solid element model was built in Abaqus. The specimen was modeled as aluminum, with different material properties in the different zones. The 16 bolts used to connect the specimen to the test frame were modeled as rigid bodies, given their much higher stiffness compared to the aluminum specimen. Solid elements C3D8R were used throughout. Three elements were used through the thickness of the plate. This allowed the elements to have aspect ratios of their sides close to 1.0 in the undeformed condition. Four elements were used on the face of the weld bead, and four elements with a slightly more elongated aspect ratio were used on the attached flat bar. A picture of the geometry of the model and the mesh is shown in Figure 62.

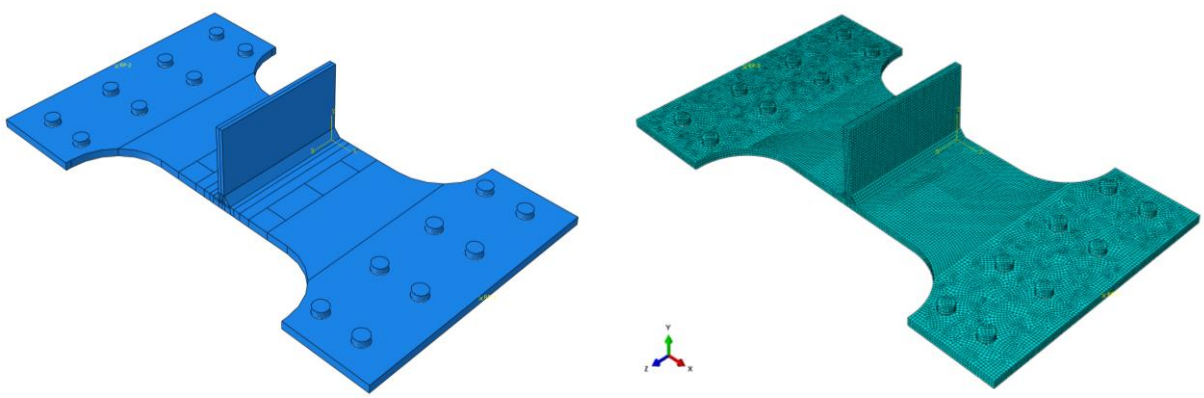

Figure 62: Abaqus FEA Model and Model Mesh

The material properties around the weld are weakened by the presence of the HAZ. To approximate this impact in the model, initial hardness values were used to adjust the average base material proof stress and Ramberg-Osgood exponent (see Equation 2) by the ratios of

hardness values. Note that the FEA analysis was done before the final specimen data analysis and that the hardness values were averaged over all sampling points. Thus, it is not possible to exactly replicate the three different replicates of each configuration. These values were assigned to the Abaqus model in strips running parallel to the welds and are shown in Table 12.

Table 12: Approximate Material Properties for Ramberg-Osgood Material Model for Continuous Welds (c) and Intermittent Welds (i)

Parameter		Base	Distance Left of Weld, mm				Distance Right of Weld, mm			
		Mat'l	0-4	5-10	11-16	17-24	0-4	5-10	11-16	17-24
5086	$\sigma_{0\ 2\%}$ MPa	230	218	214	221	229	219	217	223	229
7.9mm c.	n	8.75	8.30	8.16	8.39	8.76	8.33	8.24	8.47	8.70
5086	$\sigma_{0\ 2\%}$ MPa	230	228	222	227	229	227	223	228	230
4.8mm c	n	26	25.78	25.08	25.66	26.14	25.67	25.23	25.73	25.94
5086	$\sigma_{0\ 2\%}$ MPa	230	225	225	228	229	226	225	227	229
4.8mm i	n	26	25.38	25.45	25.73	26.14	25.59	25.45	25.70	25.87
6061	$\sigma_{0\ 2\%}$ MPa	294	210	192	239	285	206	199	250	286
7.9mm c	n	44	31.49	28.67	35.80	45.38	30.77	29.73	37.34	42.83
6061	$\sigma_{0\ 2\%}$ MPa	294	270	246	268	294	262	245	276	294
4.8mm c	n	44	40.38	36.75	40.12	44.02	39.22	36.67	41.37	44.03
6061	$\sigma_{0\ 2\%}$ MPa	294	275	261	282	294	278	259	277	292
4.8mm i	n	44	41.14	39.00	42.26	44.06	41.54	38.72	41.45	43.65

To approximate the welding residual stresses and deformations, a thermal cycle load case was introduced where the model was subjected to a welding profile, and the resulting stresses and deformed shape were used as the starting point for the load-extension simulation. This initial thermal loading was performed with fixed mechanical boundary conditions removed from the weld region to best approximate the actual construction process where these welds were made when the specimen was part of a larger structure that would offer significant restraint. The specimen was initially set to room temperature, 20 degrees Celsius. Then, a weld pass was roughly simulated by increasing the temperature in the weld bead to 550 degrees Celsius. As the goal of this step was to get approximate residual stresses and deformation, not model the change in microstructure with heat input, a welding torch pattern was not used; instead, uniform heating was assumed. Then the specimen was allowed to cool down to 20 degrees Celsius again. The specimen was deformed with about a 0.5 degree angular deformation, and significant residual stresses built up near the center of the weld, nearing the magnitude of the proof stress, as shown in Figure 63 and Figure 64.

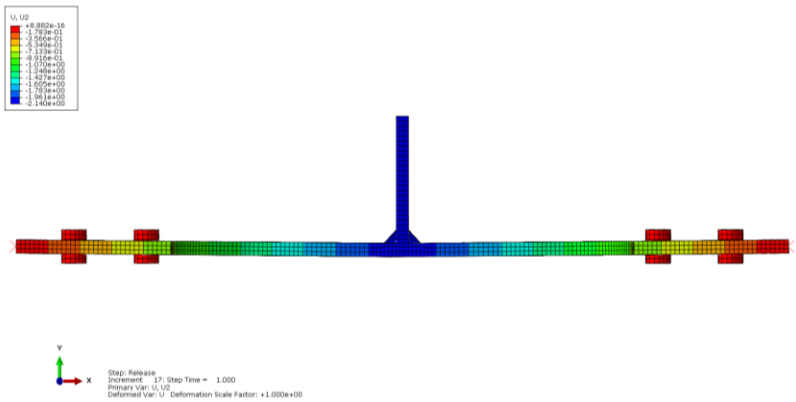

Figure 63: Vertical Deformations After Welding Simulation, Maximum about 2mm with Corresponding Angle of 0.5 Degrees from Flat

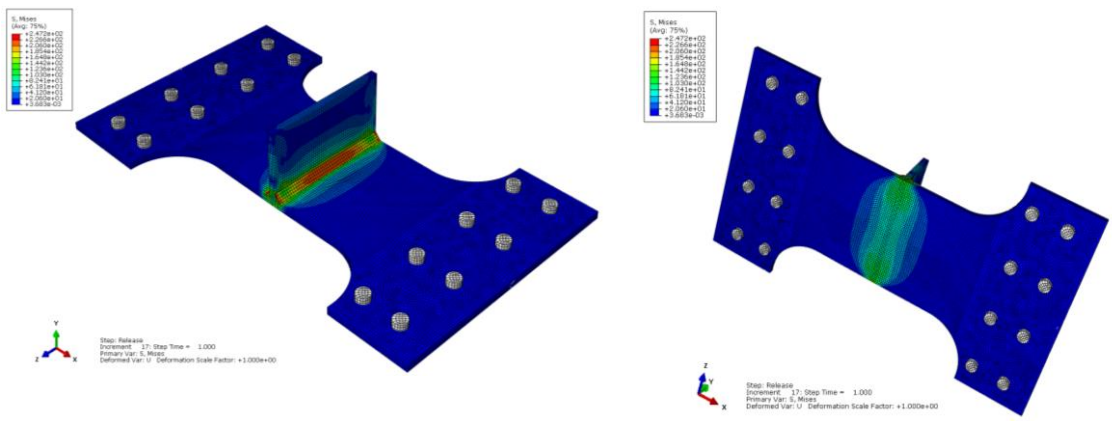

Figure 64: Residual Stresses After Welding Simulation, von Mises with Peak Red Color about 250 MPa

After performing the thermal simulation, the model with the resulting deformations and residual stresses was then loaded in tension. To replicate the clamped conditions in the test rig, the portion of the specimen in the grips was constrained out-of-plane with full fixity and constrained in-plane perpendicular to the loads. Then, prescribed deflections in the direction of tension were applied to one set of bolts, while the other set of bolts was fully fixed. The boundary conditions are shown in Figure 65.

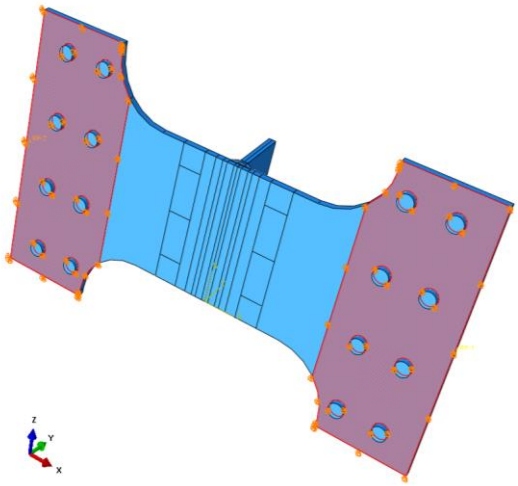

Figure 65: Boundary Conditions for Tensile Extension Load Steps in FEA Model

6.2 FEA Results

With the initial deformations, residual stresses, and boundary conditions, the FEA analysis was run to simulate the load-extension behavior of the specimen. As the FEA material model had no fracture or rupture criteria (Ramberg-Osgood stress-strain relationship applied at any strain value), the failure of the specimen could not be captured by this analysis. However, the mesh density was sufficient that local thinning (beginning of necking) and deformation of the HAZ could be modeled, resulting in a peak in the load-extension curve. As the FEA analysis was run before the final post-processing corrections for specimen rotation (as discussed in Section 5.3), a simple average of the displacement over the three pairs of markers on each side of the weld was used to compare to the average nodal displacement at a similar location in the FEA model. For the 5086 7.9mm continuous weld, a stress plot of the FEA model and the load-extension comparison to the experiment are shown in Figure 66 and Figure 67.

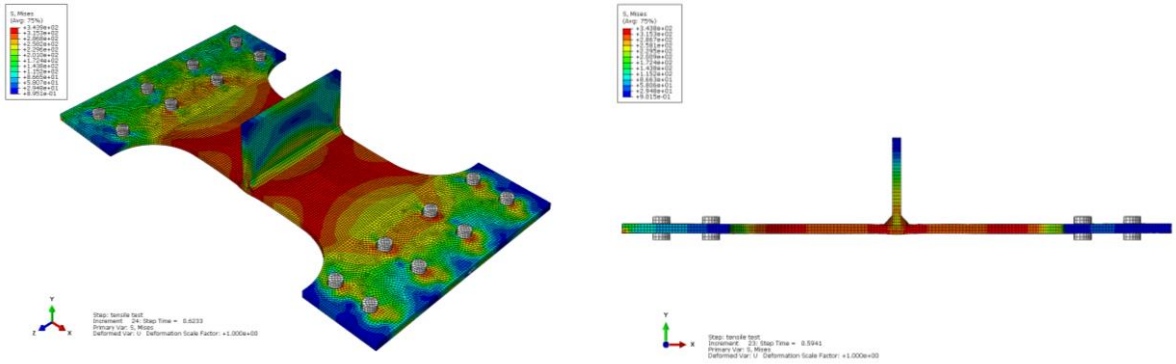

Figure 66: von Mises Stress State Near Peak Load, 5086 7.9mm Continuous Welds, Red Colors About 345 MPa

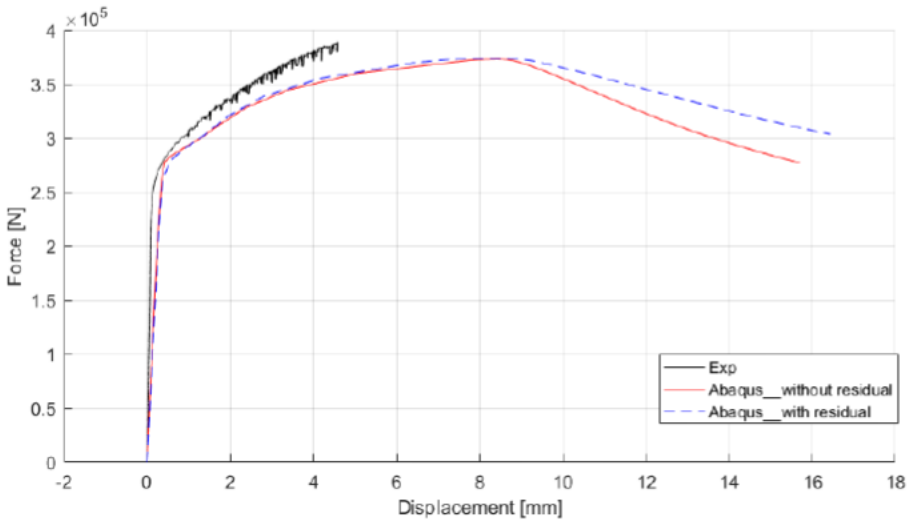

Figure 67: Load-Extension Comparison Between Simplified Experimental Average Displacement and FEA Model, 5086 7.9mm Continuous Welds

Overall, the comparison between the FEA and the experiment is encouraging. The FEA model closely follows the overall shape of the load-extension curve and comes close to the peak resisting force, although it places it at a larger strain value by almost a factor of 2.0. The FEA model predicts a flatter plateau in the load-extension behavior; this could be a result of idealizing the HAZ into four wide bands when in the experiment, a narrower weaker zone would result in a higher effective strain and stress in that region. Such a higher strain would lead to the steeper load-extension curve shown. Interestingly, the residual stresses do not seem to have a large impact on the weld response until well after the peak load is reached. Based on this finding, similar runs were made for the remaining specimens, but the residual stress thermal step, which was very time-consuming to calculate, was not included. The load-extension comparisons are shown in Figure 68 through Figure 72.

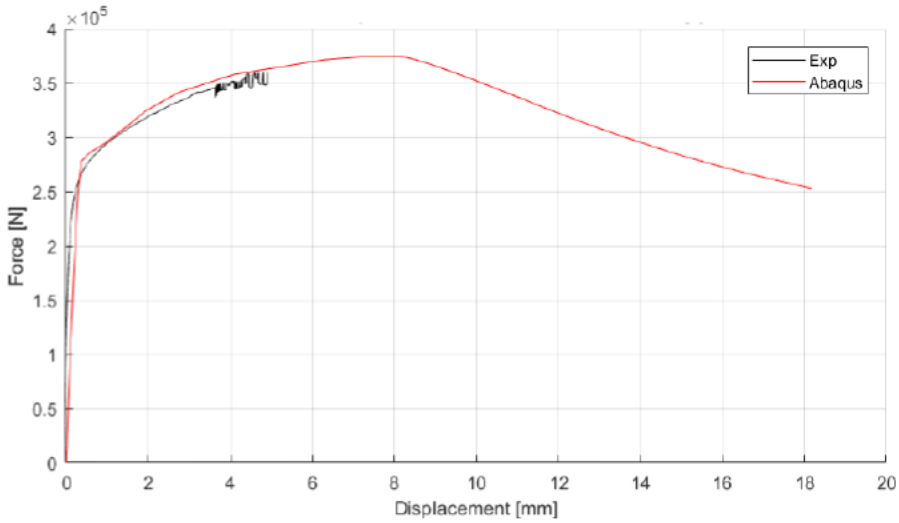

Figure 68: Load-Extension Comparison Between Simplified Experimental Average Displacement and FEA Model, 5086 4.8mm Continuous Welds

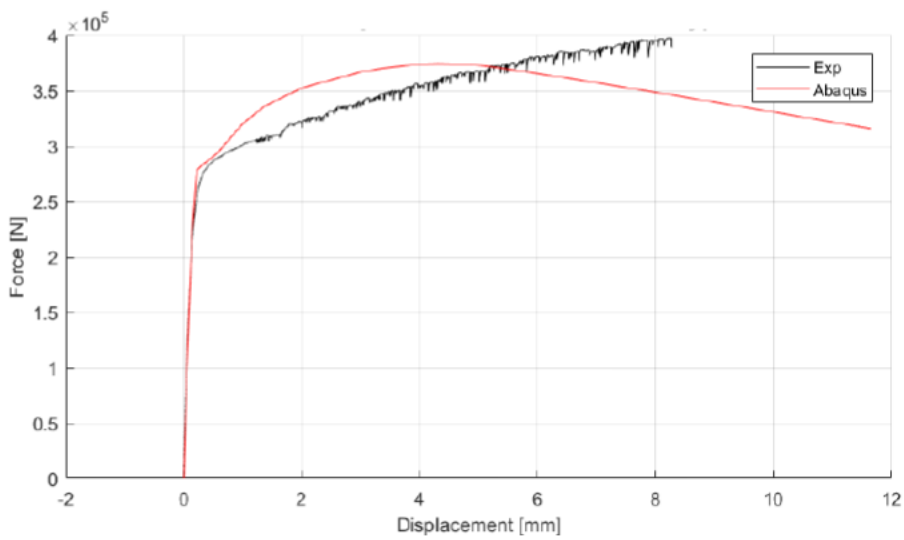

Figure 69: Load-Extension Comparison Between Simplified Experimental Average Displacement and FEA Model, 5086 4.8mm Intermittent Welds

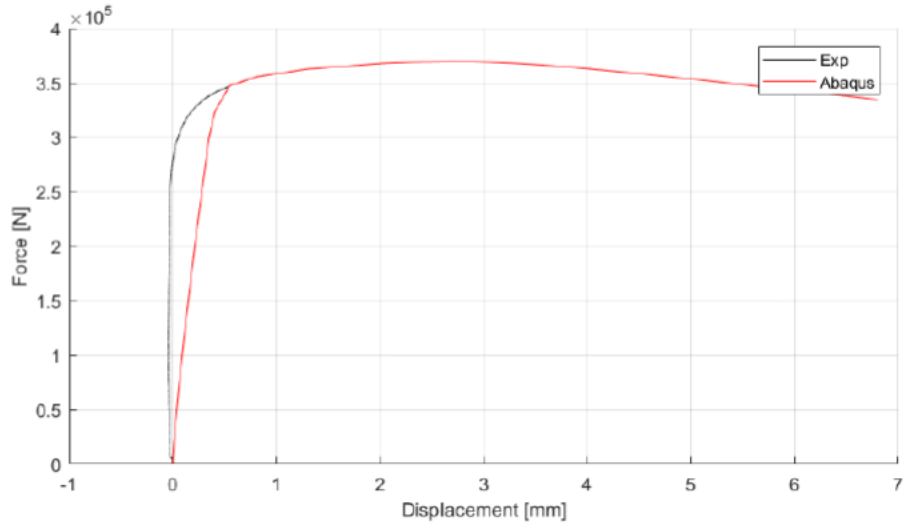

Figure 70: Load-Extension Comparison Between Simplified Experimental Average Displacement and FEA Model, 6061 4.8mm Continuous Welds

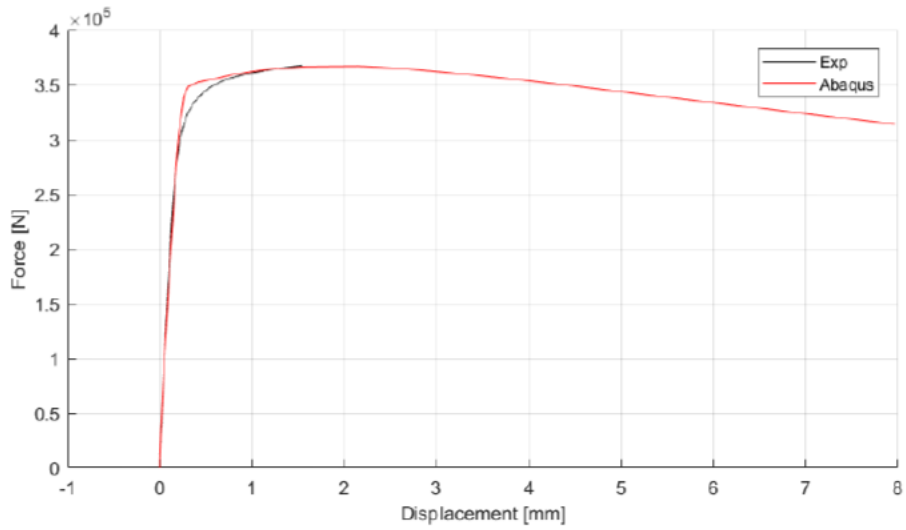

Figure 71: Load-Extension Comparison Between Simplified Experimental Average Displacement and FEA Model, 6061 4.8mm Intermittent Welds

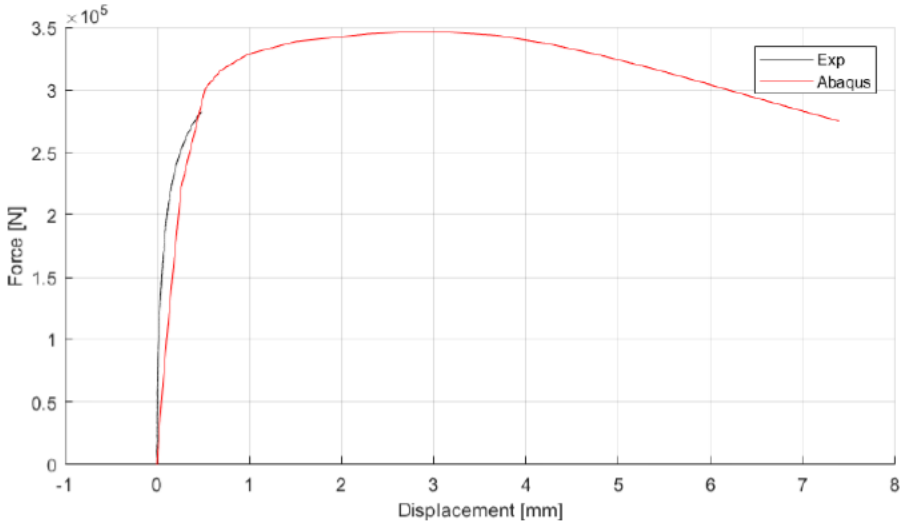

Figure 72: Load-Extension Comparison Between Simplified Experimental Average Displacement and FEA Model, 6061 7.9mm Continuous Welds

The FEA model can capture the overall shape of the load-extension curve quite well for all the different alloys and weld size combinations. A few comparisons show the slope in the plastic region is not particularly well represented in the 5086 alloys, though the overall magnitude of the resisting force is still captured with good accuracy. This could be a result of the most undermatched region not being well captured by the four different material property strips used here. Additionally, the assumption that both the proof stress and the Ramberg-Osgood exponent vary proportionally with hardness is a simplifying assumption that could miss some of the plastic behavior in the HAZ. Overall, the FEA approach can produce reasonable load-extension curves for this type of undermatched weld.

7 Discussion and Recommendations for Future Work

7.1 Discussion

Overall, the experimental results largely confirm much of the existing concerns around aluminum as a welded material. The base material properties were very consistent specimen-to-specimen. Interestingly, the 5086 proof stress values fell below the batch properties reported by the aluminum producer by just under 10%, while the ultimate stress values and both stress values for the 6061 material properties were consistent between the specimens tested at Michigan and those reported by the producer. Both grades were initially significantly above the grade minimums. Both materials showed significant anisotropic behavior. Little consideration of anisotropic properties is currently given in design codes. For allowable-stress based approaches, such concerns may not significantly enter the design code, but for more modern limit-state based approaches, or those dealing with collision, groundings, or explosive loads on the structure, such properties may need to be considered. In this work, differences between compression and tensile material properties could not be explored as compression

test fixtures were not available, but given the directional anisotropy, this is a consideration for work-hardened alloys in the 5000-series.

As expected, the aluminum strength was significantly reduced by welding; this was confirmed by both cross-weld hardness profiles and testing simulated HAZ coupons. Both the shape and peak of the material stress-strain curve were impacted. The 5086 HAZ joint showed the expected broad hardness decrease while the 6061 HAZ showed a “W” shape hardness profile, indicating that some Magnesium Silicide re-precipitation occurred in the fusion zone. The strength reduction in the HAZ also appeared tied to the amount of welding, with larger weld passes causing larger reductions in strength.

The large-scale tensile tests of the welded joints showed remarkably consistent strength across variants. Even including those that broke at the grip, the variability within each group was within 5% of the peak load. Additionally, all the failures were identical, a 45-degree ductile fracture occurring at the toe of the fillet weld and propagating into the HAZ. The failure location at the toe is likely (though we have not fully shown this) related to the stress concentration of the weld profile as well as being near the weakest region of the HAZ.

Although current design codes do not differentiate between different alloys or welding processes for HAZ effects, the data from this experiment shows that these factors do have a large impact on the strength of the joints. The results here show that the largest weld forms the lower bound of strength in each alloy. However, the 6061 specimens are much more severely impacted by the welding heat than the 5086 alloys, with a reduction on the order of 15% moving from the small continuous fillet weld to the large continuous fillet weld. The chain weld was even stronger in this alloy. This finding is not surprising given the greater reduction in the ultimate strength of the 6000-series aluminum compared to the 5000-series aluminum. This was reflected in the reduced strength seen in the simulated HAZ coupons in this study. In the context of the tension flange of a large vessel, such a strength reduction would be significant.

Compared to existing work on undermatched welds in high-strength steel alloys, aluminum has broad similarities but some significant differences. Many undermatched welds in steel are done on thick material, where the undermatched region is narrow and deep. This allows additional constraint stresses to act, increasing the joint strength, if not ductility. For the aluminum alloys tested here, the HAZ is much broader than the plate thickness, and constraint stresses, and their beneficial impact, are likely to be small. Additionally, relatively small changes in the fillet weld size produced large variations in strength in the 6061 specimens. This indicates that careful weld design and construction monitoring may be necessary for strength-critical 6061 joints.

3-D finite element models of the joint showed good ability to model the early part of the load–extension curve, even with the approximation of the material properties used here. It appeared that the simulated HAZ heat input was too low in the experimental approach used here; thus, the process of correlating stress-strain curves with specific hardness regions in the

HAZ zone could not be fully completed. While the final failure could not be modeled with the FEA approach taken here, the initial stiffness appears well-captured. However, to apply this approach in practice, a way of converting between weld size and HAZ material properties would be needed. On specimens of this size, residual stresses did not seem to have a large impact on the finite element simulation results.

In terms of experimental design, several lessons were learned from the approach taken here:

1. The process of making the hardness measurements on the cross-weld specimen took significant trial and error to achieve. In the end, an almost mirror-like finish with polishing down to the micron level was needed to get consistent results. The curves shown here were the average of four specimens; at least this number is needed as there can be odd measurements even after extensive polishing.
2. Simulating the HAZ for material coupons was done using the process outlined in prior papers for inducing HAZ – making a GTAW pass with no filler metal deposited. While this did create a HAZ, it seemed to have created a narrower HAZ based on the mechanical results shown here. This may have been a result of not including the filler metal in the GTAW pass; presumably, during the solidification of the filler metal, the base metal would be further heated, increasing the size of the HAZ. If used in future work, this method should be better characterized before applying it to test specimens. It would be valuable to make a more detailed study of the achieved thermal input vs. GTAW parameters before making the final passes on the specimens. It may also be necessary to have solidifying molten filler metal to truly capture the heat input into the base material that causes the HAZ. However, this has not yet been explored.
3. The use of load-carrying bolts to transfer the load into the specimens caused difficultly in correlating the cross-head displacement with the local strains measured closer to the weld. In the future, textured grip surfaces that are driven into the aluminum material by the clamping force of the bolt (with the load then transferred by shear, not the bolts) would work better for this sort of test.
4. The very high strength of the material also caused higher failure loads than expected. Although there was a safety factor of 1.3 on tear-out of the bolts, two of the eighteen specimens still failed this way. It appears that local deformation of the bolt holes changed the loading per bolt (not assumed in the finite element model where all bolts were loaded equally) and initiated a local failure. If a textured grip cannot be used, a higher safety factor is recommended for future tests.

Overall, the results of this experiment show that non-load carrying fillet weld connections cause localized failures in the HAZ, originating at the toe of the weld. This indicates that the tensile response of the aluminum structure may be significant for the overall response of the structure in limit-state situations. Further investigation and efficient FE modeling techniques for such joints are warranted.

7.2 Suggestions for Future Work

This work has highlighted the importance of understanding the role of under-matched HAZ in aluminum structures. During this work, several avenues for future exploration appeared worthwhile to pursue:

1. Further processing of the load-extension curves would be worthwhile. Initial investigations in this project revealed that the load-extension curves have "stiff" initial regions that corrections for out-of-plane deformations could not resolve. As such curves could help FEA model validation, more exploration of these curves would be worthwhile.
2. Examination of simplified FEA modeling procedures for such joints, including relations between weld parameters and the material properties. Simplified models such as cohesive zones should also be explored. To be able to predict the response of such joints during design, a database of likely material properties throughout the HAZ with different weld parameters would also be needed.
3. Exploration of other types of tensile limit states for welded aluminum structures. While direct tension of the HAZ, as explored here, was shown to be critical, there are other types of connections that are also worth investigating. Load-carry fillet welds for double-sided extrusions would be one example, and more complex stiffener-frame intersections would also worth exploring. Initial work on these joints in this project had failures in the grips with the current specimen design. A revised design and test plan would be welcome. Additionally, the lateral response of plates with HAZ at the boundaries or in different orientations across the span of the plate would be worth studying. Such plates are often used in locations where they need to resist slamming pressures or vehicle tire loads. The permanent set of the plating under such loads, as well as the ultimate strength of the plating before fracture in the HAZ, would both be of interest. Additionally, multi-directional loading (external lateral sea pressure along with in-plane responses) may also change the stress state in the HAZ and would be worth exploring once the basic response of such connections is well established.
4. The scope of the current study did not include making design recommendations or suggesting revisions to existing codes. Parametric studies of the performance of such joints, preferably with validated numerical models, to help validate existing design approaches would be worthwhile. A careful relation between the response of the joint and the assumed material parameters is essential. This would help remove the confusion arising from the use of different gauge lengths for setting HAZ material properties in existing regulations, even though the reasons for the different strengths at different gauge lengths are clear.

8 Conclusions

Undermatched HAZ in aluminum structures pose several concerns, primarily related to the localization of plastic deformations in the narrow undermatched regions. This can make the overall structural response appear almost brittle, with fracture occurring at low global strains in the structure, even though the actual failure in the structure is ductile in the HAZ. The existing literature indicates that this type of failure is a concern in welded aluminum structures but has

not specifically investigated the types of connections common in the marine industry. This work started to address this gap by looking at non-load carrying fillet welds. Such connections are common where transverse frames meet the shell plating of the vessels, and the resulting HAZ region is oriented perpendicular to the primary stress field on the vessel. A series of 18 specimens, varying weld size, and alloy type were tested under this program. Additionally, material characterization of the base material and weld regions was performed. The results showed striking consistency between samples but confirmed that the HAZ significantly impacts the strength of the connection; the failure will be localized in the HAZ region as expected for this type of connection and may influence the overall response of the structure. FEA was shown to be able to approximate the response of these details with acceptable accuracy. Further investigations into these connections and modeling approaches appear warranted.

9 Acknowledgments

The author wishes to acknowledge the support of Dr. Paul Hess, Office of Naval Research Code 331, for supporting this work, the helpful comments of the Ship Structure Committee PTC, especially David Kihl, Ken Nahshon, and Bob Sielski. The author is grateful to Matthew Unger and Metal Shark Marine for donating material and labor to fabricate the test panels and Claire Wincott, Renee Wiwel, Kaihua Zhang, Hung-Chun Lin, and Professor Jason McCormick for assistance with the test preparation, execution, and post-processing and report writing.

10 References

[1] R. Sielski, “Aluminum Structure Design and Fabrication Guide,” Ship Structure Committee, Washington, DC, SSC-452, May 2007.

[2] H. Hill, J. Clark, and A. Brungraber, “Design of Welded Aluminum Structures,” *J. Struct. Div. Proc. ASCE*, vol. 86, no. ST6 (June), pp. 101–124, 1960.

[3] K. Satoh and M. Toyoda, “Joint Strength of Heavy Plates with Lower Strength Weld Metal,” *Weld. J. Res. Suppl.*, no. September, pp. 311s–319s, 1975.

[4] K. Satoh and M. Toyoda, “Static Tensile Properties of Welded Joints Including Soft Interlayer,” *Trans. Jpn. Weld. Soc.*, no. April, pp. 7–12, 1970.

[5] R. J. Dexter and M. Ferrell, “Optimum Weld-Metal Strength for High-Strength Steel Structures,” Ship Structure Committee, Washington D.C., SSC-383, Jul. 1995.

[6] R. L. Tregoning, “Experimental Investigation of Mismatched Weld Joint Performance,” *Fatigue Fract. Mech. ASTM STP 1296*, vol. 27, pp. 427–450, 1997.

[7] M. Scott and M. Gittos, “Tensile and Toughness Properties of Arc-Welded 5083 and 6082 Aluminum Alloys,” *Weld. J. Res. Suppl.*, pp. 243s–252s, Sep. 1983.

[8] L. Ovreas, C. Thaulow, and M. Hval, “Effect of Geometry and Size on the Mechanical Properties of AlMgSi1 Weldments,” 1992.

[9] M. Hval, R. Johnsen, and C. Thaulow, “Strength and Deformation Properties of Welded Aluminium Structures With Reference to Local Design and Material Properties,” 167-182, 1995.

[10] V. Malin, “Study of metallurgical phenomena in the HAZ of 6061-T6 aluminum welded joints,” *Weld. J.*, vol. 74, no. 9, pp. 305s–318s, 1995.

[11] M. Matusiak, “Strength and Ductility of Welded Structures in Aluminium Alloys,” PhD Thesis, Norwegian University of Science and Technology, Trondheim, 1999.
[12] M. Matusiak and P. K. Larsen, “Strength and Ductility of Welded Connections in Aluminium Alloys,” in *Joints in Aluminium - INALCO 98*, Cambridge, 1998, pp. 299–310.
[13] T. Chan and R. Porter Goff, “Welded aluminium alloy connections: a simplified plastic model,” *Proc. Inst. Civ. Eng. Struct. Build.*, vol. 140, no. May, pp. 161–168, 2000.
[14] A. K. Lakshminarayanan, V. Balasubramanian, and K. Elangovan, “Effect of welding processes on tensile properties of AA6061 aluminium alloy joints,” *Int. J. Adv. Manuf. Technol.*, vol. 40, no. 3–4, pp. 286–296, Jan. 2009, doi: 10.1007/s00170-007-1325-0.
[15] M. Collette, “The impact of fusion welds on the ultimate strength of aluminum structures,” in *10th International Symposium on Practical Design of Ships and Other Floating Structures (PRADS 2007)*, Houston, Texas, 2007, vol. 2, pp. 944–952.
[16] Z. L. Zhang, J. Ødegård, O. R. Myhr, and H. Fjær, “From microstructure to deformation and fracture behaviour of aluminium welded joints – a holistic modelling approach,” *Comput. Mater. Sci.*, vol. 21, no. 3, pp. 429–435, Jul. 2001, doi: 10.1016/S0927-0256(01)00181-1.
[17] T. Wang, “Modelling of welded thin-walled aluminium structures,” PhD Thesis, Norwegian University of Science and Technology, Trondheim, 2006.
[18] T. Wang, O. S. Hopperstad, O.-G. Lademo, and P. K. Larsen, “Finite element analysis of welded beam-to-column joints in aluminium alloy EN AW 6082 T6,” *Finite Elem. Anal. Des.*, vol. 44, no. 1–2, pp. 1–16, Dec. 2007, doi: 16/j.finel.2007.08.010.
[19] T. Wang, O. S. Hopperstad, O.-G. Lademo, and P. K. Larsen, “Finite element modelling of welded aluminium members subjected to four-point bending,” *Thin-Walled Struct.*, vol. 45, no. 3, pp. 307–320, 2007.
[20] T. Wang, O. S. Hopperstad, P. K. Larsen, and O.-G. Lademo, “Evaluation of a finite element modelling approach for welded aluminium structures,” *Comput. Struct.*, vol. 84, no. 29–30, pp. 2016–2032, 2006.
[21] C. Dørum, O.-G. Lademo, O. R. Myhr, T. Berstad, and O. S. Hopperstad, “Finite element analysis of plastic failure in heat-affected zone of welded aluminium connections,” *Comput. Struct.*, vol. 88, no. 9, pp. 519–528, May 2010, doi: 10.1016/j.compstruc.2010.01.003.
[22] J. A. Vargas, J. E. Torres, J. A. Pacheco, and R. J. Hernandez, “Analysis of heat input effect on the mechanical properties of Al-6061-T6 alloy weld joints,” *Mater. Des. 1980-2015*, vol. 52, pp. 556–564, Dec. 2013, doi: 10.1016/j.matdes.2013.05.081.
[23] J. V. Jakobsen, “Microstructure and Mechanical Properties of Welded AA6082 Aluminium Alloys,” *104*, 2016, Accessed: Jan. 08, 2019. [Online]. Available: https://brage.bibsys.no/xmlui/handle/11250/2406949.
[24] R. Deekhunthod, “Weld Quality in Aluminum Alloys,” Uppsala Universitet, Uppsala, Sweden, 2014.
[25] N. Nazemi, “Identification of the Mechanical Properties in the Heat-Affected Zone of Aluminum Welded Structures,” PhD Thesis, University of Windsor, Windsor, Canada, 2015.
[26] Brando Giuseppe, Sarracco Gianluca, and De Matteis Gianfranco, “Strength of an Aluminum Column Web in Tension,” *J. Struct. Eng.*, vol. 141, no. 7, p. 04014180, Jul. 2015, doi: 10.1061/(ASCE)ST.1943-541X.0001138.

[27] P. Wiechmann, H. Panwitt, H. Heyer, M. Reich, M. Sander, and O. Kessler, “Combined Calorimetry, Thermo-Mechanical Analysis and Tensile Test on Welded EN AW-6082 Joints,” *Materials*, vol. 11, no. 8, p. 1396, Aug. 2018, doi: 10.3390/ma11081396.
[28] P. A. Stathers, A. K. Hellier, R. P. Harrison, M. I. Ripley, and J. Norrish, “Hardness-tensile property relationships for HAZ in 6061-T651 aluminum,” *Weld. J.*, vol. 93, pp. 301s–311s, 2014.
[29] L. Zheng, D. Petry, H. Rapp, and T. Wierzbicki, “Mode I fracture of large-scale welded thin-walled AA 6061 extruded panels,” *Thin-Walled Struct.*, vol. 47, no. 4, pp. 375–381, Apr. 2009, doi: 10.1016/j.tws.2008.09.005.
[30] L. Zheng, D. Petry, H. Rapp, and T. Wierzbicki, “Characterization of material and fracture of AA6061 butt weld,” *Thin-Walled Struct.*, vol. 47, no. 4, pp. 431–441, Apr. 2009, doi: 10.1016/j.tws.2008.08.008.
[31] L. Zheng, D. Petry, H. Rapp, and T. Wierzbicki, “Mode III fracture of a large-scale welded extruded aluminum panel,” *Thin-Walled Struct.*, vol. 46, no. 11, pp. 1262–1273, Nov. 2008, doi: 10.1016/j.tws.2008.02.008.
[32] B.-Q. Chen and C. Guedes Soares, “Numerical Investigation on Weld Induced Imperfections in Aluminium Ship Plates,” p. V003T02A070, Jun. 2018, doi: 10.1115/OMAE2018-77655.
[33] P. B. Woelke, B. K. Hiriyur, K. Nahshon, and J. W. Hutchinson, “A practical approach to modeling aluminum weld fracture for structural applications,” *Eng. Fract. Mech.*, vol. 175, pp. 72–85, Apr. 2017, doi: 10.1016/j.engfracmech.2017.02.010.
[34] AWS, “D3.7:2004 Guide for Aluminum Hull Welding,” Miami, Florida: American Welding Society, 2004.
[35] The Aluminum Association, *Aluminum Design Manual*. Arlington, VA: The Aluminum Association, 2010.
[36] ASTM, “Standard Test Methods for Tension Testing of Metallic Materials,” in *ASTM Standard E8/EM8*, West Conshohocken, PA, USA: ASTM International, 2011.
[37] ASTM, “B 209-06 Standard Specification for Aluminum and Aluminum -alloy Sheet and Plate,” West Conshohocken, PA: ASTM International, 2006.
[38] ASTM, “B 928 - 06 Standard Specification for High-Magnesium Aluminum-Alloy sheet and Plate for Marine Service and Similar Environments,” West Conshohocken, PA: ASTM International.
[39] P. Sensharma, M. Collette, and J. Harrington, “Effect of Welded Properties on Aluminum Structures,” Ship Structure Committee, Washington, DC, USA, SSC-460, Jan. 2011.
[40] M. L. Sharp, *Behavior and design of aluminum structures*. New York: McGraw-Hill, 1993.
[41] J.-H. Zhu and B. Young, “Effects of transverse welds on aluminum alloy columns,” *Thin-Walled Struct.*, vol. 45, no. 3, pp. 321–329, Mar. 2007, doi: 10.1016/j.tws.2007.02.008.